Efficient production of acetate from inorganic carbon (HCO3–) in microbial electrosynthesis systems incorporating Ag3PO4/g-C3N4 anaerobic photo-assisted biocathodes

October 20, 2020 R1

Submitted to Appl Catal B-Environ

Efficient production of acetate from inorganic carbon (HCO_3^-) in microbial electrosynthesis systems incorporating Ag_3PO_4/g-C_3N_4 anaerobic photo-assisted biocathodes

Weifeng Kong[a], Liping Huang[a,*], Xie Quan[a], Zongbin Zhao[b], Gianluca Li Puma[c,*]

[a]Key Laboratory of Industrial Ecology and Environmental Engineering, Ministry of Education (MOE), School of Environmental Science and Technology, Dalian University of Technology, Dalian 116024, China

[b]State Key Lab of Fine Chemicals, Liaoning Key Lab for Energy Materials and Chemical Engineering, School of Chemical Engineering, Dalian University of Technology, Dalian 116024, China

[c]Environmental Nanocatalysis & Photoreaction Engineering, Department of Chemical Engineering, Loughborough University, Loughborough LE11 3TU, United Kingdom

Corresponding authors:

lipinghuang@dlut.edu.cn (L. Huang)

g.lipuma@lboro.ac.uk (G. Li Puma)

The authors declare no competing financial interest.

Abstract

The efficient production of acetate from HCO_3^- by the nonphotosynthetic bacterium *Serratia marcescens* Q1 is demonstrated in an anaerobic, photo-assisted, microbial electrosynthesis (MES) system incorporating a Ag_3PO_4/g-C_3N_4 biocathode. The Ag_3PO_4/g-C_3N_4 formed a Z-scheme photocatalytic heterojunction structure with enhanced redox capacity. The photocorrosion of Ag_3PO_4 was inhibited by the production of H_2O_2 in-situ, through water oxidation driven by the photogenerated holes on the Ag_3PO_4 valence band. The photoinduced electrons on the conduction band of g-C_3N_4 instead produced H_2, which was metabolized by the Q1 electrotroph with HCO_3^- to produce acetate at a rate of 5.4 mM/d with a $CE_{acetate}$ of 93% at a current density of 3.3 A/m^2. The MES accumulated up to 81.0 mM with a $CE_{acetate}$ of 89% over 16 days continuous operation. This study provides a sustainable and feasible strategy for inhibiting the photocorrosion of Ag_3PO_4 and thus achieve efficient acetate production from HCO_3^- in photo-assisted MESs biocathodes.

Keywords: microbial electrosynthesis; photocatalytic; in-situ H_2O_2; silver phosphate; graphitic carbon nitride

1 Introduction

Microbial electrosynthesis (MES) systems incorporating photocatalytic biocathodes have been demonstrated as a promising sustainable technology for the production of valuable products (e.g., acetate) from the reduction of inorganic carbon (HCO_3^-) [1-4] which in turn originates from CO_2 emissions. For example, cadmium sulfide (CdS) immobilized on a photocathode and assembled with the nonphotosynthetic CO_2-reducing bacterium *Moorella thermoacetica* [2,5], indium phosphide (InP) combined with *Methanosarcina barkeri* [6], or WO_3/MoO_3/g-C_3N_4 matched with *Serratia marcescens* [7], have been shown to successfully catalyze the production of acetate or methane from inorganic carbon. However, more effort is needed to develop more active photocatalysts, in order to broaden the field of application of photo-assisted biocathodes in MESs.

Among a wide range of possible photocatalysts, silver phosphate (Ag_3PO_4) has shown promising results due to its desirable band gap (2.36 eV), low-toxicity, and its highly positive valence band position [8-11]. On the other hand, graphitic carbon nitride (g-C_3N_4) is a low cost visible-light responsive semiconductor photocatalyst (band gap about 2.7 eV), with a high chemical stability and excellent reduction properties due to its relatively negative conduction band (CB) edge position (−1.2 eV vs. standard hydrogen electrode, SHE) [12-15]. Furthermore, hybridizing Ag_3PO_4 with g-C_3N_4 creates a Z-scheme photocatalytic mechanism, which has been shown to enhance the photocatalytic evolution of oxygen from water [16] and the conversion of CO_2 into CO, methane, methanol and ethanol [17]. Although Ag_3PO_4/g-C_3N_4 has

shown significant light capture and charge separation properties, the photocatalytic reduction of CO_2 over this inorganic composite material still suffer from further challenges, particularly in terms of product selectivity. In addition, the long-term stability of the Ag rare metal in the composite has not been entirely fulfilled [16-17]. By comparison, biological organisms engage an army of enzymes and reductive pathways to produce long-chain hydrocarbons from naturally available constituents including CO_2, H_2O and N_2. Thus, the combination of inorganic light-harvesters photocatalyst and whole-cell biocatalysts can be strategically deployed to exploit the most salient attributes of each component [18]. However, neither Ag_3PO_4 nor the composite Ag_3PO_4/g-C_3N_4 have been explored as photocatalysts in MESs.

One important aspect that affects the photocatalytic activity of Ag_3PO_4 is its chemical stability, which is severely limited by the photocorrosion process that occurs through the reduction of Ag(I) to Ag(0) [19-20]. One study has shown improved stability of Ag_3PO_4/g-C_3N_4 heterojunctions by supplementing the reaction system with an external electron acceptor such as H_2O_2. This way, H_2O_2 outcompeted Ag(I) for the scavenging of photoinduced electrons due to a higher redox potential (Reaction 1), thus suppressed the photoetching of Ag_3PO_4 (Reaction 2) [21].

$$H_2O_2 + 2H^+ + 2e^- \rightarrow 2H_2O \qquad E^0 = +1.78\ V \qquad (1)$$

$$Ag^+ + e^- \rightarrow Ag \qquad E^0 = +0.80\ V \qquad (2)$$

$$2H_2O \rightarrow H_2O_2 + 2H^+ + 2e^- \qquad (3)$$

$$2H^+ + O_2 + 2e^- \rightarrow H_2O_2 \qquad (4)$$

$$photocatalyst + h\nu \rightarrow h^+ + e^- \qquad (5)$$

90 $$2H_2O + 2h^+ \rightarrow H_2O_2 + 2H^+ \quad (6)$$

91 In this study, rather than adding H_2O_2 from an external source, we are proposing
92 the idea that the stability of Ag_3PO_4 and Ag_3PO_4/g-C_3N_4 heterojunctions can be
93 maintained by designing an anaerobic photocatalytic system which can produce H_2O_2
94 in-situ at the photo-assisted biocathode surface. In a photoelectrocatalytic system
95 H_2O_2 can be produced either through an electrochemical route by water oxidation at
96 the anode or by oxygen reduction reaction near the cathode [22] (Reactions 3 – 4), or
97 through the photocatalytic route [23-24] (Reactions 5 – 6). The anaerobic atmosphere
98 maintained in the Ag_3PO_4/g-C_3N_4 anaerobic photo-assisted biocathode excludes the
99 electrochemical reduction of oxygen on the cathode. Thus, it is reasonable to assume
100 that an anaerobic photo-assisted MES biocathode incorporating Ag_3PO_4/g-C_3N_4
101 should be able to produce H_2O_2 in-situ via the photocatalytic route as extensively
102 reported [23-25] which would successfully inhibit the photocorrosion of Ag_3PO_4, and
103 thus efficiently catalyze the conversion of inorganic carbon to acetate.

104 Under this background, in this study a Ag_3PO_4/g-C_3N_4 photocathode was
105 anaerobically constructed and incorporated in a MES operated with *Serratia*
106 *marcescens* Q1 bacterium species to investigate the production of acetate from
107 inorganic carbon. In this bio-electro-catalytic system, photo-induced electrons on the
108 conduction bands of Ag_3PO_4/g-C_3N_4 are expected to favor hydrogen evolution under
109 anaerobic conditions, which can then be metabolized by *S. marcescens* with HCO_3^- to
110 produce acetate. Simultaneously, the rate of photocorrosion of Ag_3PO_4 in the
111 biocathode and thus its long-term stability, was examined as a function of the

protecting role exerted by the H_2O_2 produced in-situ on the biocathode surface. Multiple methods including photoluminescence (PL), photo-current, ultraviolet-visible diffuse reflection spectra (UV–vis DRS), scanning electron microscopy equipped with an energy dispersive X-ray spectroscopy (SEM-EDS), X-ray diffraction (XRD), X-ray photoelectron spectroscopy (XPS), electron spin resonance (ESR), cyclic voltammetry (CV) and electrochemical impedance spectroscopy (EIS) were extensively used to characterize the performance of the bio-electro-catalytic system and the photoetching process of Ag_3PO_4, whereas high-sensitivity flow cytometry was used to evaluate the electrotrophic viability in the presence of the photocatalyst and under light irradiation conditions. The predominant photocatalytic mechanisms were further investigated through active species trapping experiments to determine the main reactive radical species in the system.

2 Materials and methods

2.1. Synthesis of g-C_3N_4 and Ag_3PO_4/g-C_3N_4 powders, and preparation of Ag_3PO_4/g-C_3N_4 photocathodes

Preliminary experiments of transient photocurrent response of Ag_3PO_4/g-C_3N_4 composites prepared using different methods were performed to select the most suitable preparation method (Supporting Information (SI), Fig. S1). The preparation method reported by Zhang et al. [26] was selected due to its simplicity and highest photocurrent response. Therefore, the synthesis of g-C_3N_4 and Ag_3PO_4/g-C_3N_4 powders was as reported by Zhang et al. [26] and briefly described in SI. The

134 Ag_3PO_4/g-C_3N_4 photocathode was prepared through an impregnation method:
135 Designed amounts of Ag_3PO_4/g-C_3N_4 powders (0.5 g, 1.0 g, 1.5 g, 2.0 g) were firstly
136 dispersed in 1000 mL deionized water with 10 h ultrasonication at room temperature.
137 The suspensions were centrifuged for 10 min at 5000 r/min to obtain supernatants.
138 The 2.0 cm × 2.0 cm × 0.25 cm graphite felts (Sanye Co., Beijing, China) were
139 immersed in the supernatants for 12 h and dried at 60 °C in an oven overnight. The
140 amount of Ag_3PO_4/g-C_3N_4 loaded onto the cathode was estimated from the difference
141 between the initial and the residual amounts of Ag_3PO_4/g-C_3N_4 in solution. Finally,
142 the cathodes were calcined at 300 °C for 2 h with a heating rate of 2 °C/min in a
143 muffle furnace. The Ag_3PO_4 and g-C_3N_4 loaded cathodes were also prepared as above.
144
145 *2.2. Reactor construction, electrotroph inoculation and operation*
146 The dual-chamber reactor was constructed using cubic polymethyl methacrylate
147 blocks forming anodic and cathodic chambers with internal volumes equal to 28 ml
148 each. The effective working volume of each chamber was 26 mL, and the two
149 chambers were separated by a cation exchange membrane (CMI-7000 Membranes
150 International, Glen Rock, NJ). The above prepared Ag_3PO_4/g-C_3N_4 graphite felt was
151 used as cathode, whereas a carbon rod served as anode. A saturated calomel electrode
152 (SCE, +241 mV versus standard hydrogen electrode (SHE)) was used as cathode
153 reference electrode. All electrode potentials were reported versus SHE.
154 The anode chamber was inoculated with an effluent collected from acetate-fed
155 microbial fuel cells supplemented by an equivalent volume of nutrient solution as

156 previously reported [27]. The cathode chamber instead was inoculated with the
157 nonphotosynthetic electrotroph of *Serratia marcescens* Q1, which was isolated from
158 anaerobic biocathodes of separate bioelectrochemical systems fed by the sole carbon
159 source of inorganic carbon and capable of anaerobically metabolizing inorganic
160 carbon to acetate [7].

161 Catholyte containing NH_4Cl (2.1 mM), KH_2PO_4 (0.09 mM), $NaHCO_3$ (23.8 mM),
162 vitamins 0.6 mL/L and mineral 0.6 mL/L, was sparged with N_2 gas for 15 min in an
163 anaerobic glovebox (YQX-II, Xinmiao, Shanghai) before being transferred into the
164 anaerobic cathodic chamber. The initial pH was adjusted to 5.8 with the addition of
165 10% HCl [7], and the conductivity was regulated to 103 mS/cm with 0.6 M KCl [1].
166 After 24 h incubation in a sterile medium, the Q1 electrotroph was harvested and was
167 inoculated to the cathodic chamber at a final OD_{600} of 0.35, which was selected as a
168 tradeoff between efficient biocatalysis and light absorption on the Ag_3PO_4/g-C_3N_4
169 cathode surface. In fact, it is known that a higher amount of electrotrophs confers
170 superior bioelectrocatalytic activity and stability, whereas a thinner and more
171 transparent or patchy electrotrophs layer allows for greater cathode photon absorption
172 and PL efficiency [6].

173 The reactors were run in fed-batch operation. The cathode worked at a potential
174 of –1.1 V versus SHE [7] and under a light intensity of 26.9 kLux through a 100 W
175 iodine tungsten lamp [27]. The intensity of light was measured with an illuminometer
176 (TES-1330A, Taiwan, China). The lamp was refrigerated by a cool-fan and the
177 reactors were surrounded in a jacket with a continuous circulation of water to

maintain the temperature of the reaction chambers isothermal at 25 ± 3 °C [27]. All the operation was repeated at least three times and data were collected after the first operational cycle [7].

The performance of the MES was assessed against five control experiments: a) the abiotic control, which established the role played by the electrotroph on the methabolism of HCO_3^- and H_2; b) the dark control, which assessed the impact of light irradiation on the photocathode performance; c) the open circuit conditions (OCCs) control, which elucidated the impact of the electrochemical process (closed circuit conditions, CCCs) on either acetate production or on the protective role on Ag_3PO_4 exerted by H_2O_2 produced in-situ; d) the fourth control confirmed the roles performed by the bare graphite felt, the Ag_3PO_4/graphite felt, and the g-C_3N_4/graphite felt on the photocatalytic process; e) the fifth abiotic control performed in the absence of irradiation, demonstrated the impact of light irradiation in the production of H_2.

2.3. Characterizations and electrochemical measurements

The morphologies of the photocathodes with or without the electrotrophic biofilms were examined by a SEM (Nova NanoSEM 450, FEI company, USA) equipped with an EDS (X-MAX 20-50 mm^2, Oxford Instruments, UK) and a TEM (Tecnai G2 F30 S-Twin, FEI, USA) at an accelerating voltage of 200 kV. The crystal structure and phase composition of the obtained samples were determined by XRD using a powder X-ray diffractometer (XRD-6000, Shimadzu, Japan) equipped with Cu K_α radiation (40 kV, 50 mA). Fourier transform infrared (FTIR) spectra were

collected by using a Bruker VERTEX 70 FTIR (Germany) apparatus. The zeta potential of the samples was determined with a Zetasizer Nano ZS90 (Malvern, UK). The PL spectra were recorded with a fluorescence spectrophotometer (F-4500, Hitachi, Japan) with a laser (λ = 365 nm) at room temperature. The UV-vis DRS spectra of the semiconductor photocatalysts were recorded with an Agilent HP 8453 UV-vis spectrophotometer. The photocurrent response measurements were conducted in a solution of 0.1 M Na_2SO_4 with a light illuminance of 26.9 kLux to examine the photocatalytic property of the cathode [27-28]. ESR (Bruker A200, Karlsruhe, Germany) analysis was employed to detect oxygen-containing radicals formed in the MES. 5,5-dimethyl-1-pyrroline-N-oxide (DMPO) was used as the spin-trapping agent [16,29].

Cyclic voltammetry (CV) and electrochemical impedance spectroscopy (EIS) were carried out to evaluate the electrochemical performance of the photo-assisted biocathode of MESs. CV was performed using a potentiostat at a low scan rate of 0.1 mV/s (BioLogic, VSP, France) in the range from −1.4 V to 0.1 V vs. SHE. EIS was recorded in the frequency range from100 kHz to 0.01 Hz with an amplitude of 5 mV at −1.1 V vs. SHE. Both CV and EIS were performed with a three-electrode system. The cathode electrode was employed as working electrode, the SCE served as reference electrode and a Pt foil electrode was used as counter electrode [30]. A Zsimpwin software was plotted to acquire the equivalent circuit and the values of different resistances.

222 *2.4. Analysis and calculations*

223 The concentrations of acetate and the residual hydrogen in the headspace of the
224 cathodic chamber were measured with a gas chromatograph (GC7900, Tianmei,
225 China), and the results of H_2 were normalized to the volume of the catholyte and
226 operational time ($m^3/m^3/d$). The concentration of inorganic carbon in the catholyte
227 was determined according to the national standard method (DZ/T 0064.49-93) and the
228 consumption of inorganic carbon (%) was calculated according to the difference
229 between the initial and the final inorganic carbon concentrations in the catholyte,
230 divided by the initial inorganic carbon concentration. The concentration of Ag_3PO_4
231 (%) leached in the catholyte was measured by atomic absorption spectroscopy
232 (AAnalyst 700, PerkinElmer), while the amount leached was calculated from the
233 amount of Ag_3PO_4 in the catholyte divided by the initial amount of Ag_3PO_4 on the
234 cathode. The in-situ produced H_2O_2 was measured by titanyl sulfate
235 spectrophotometric method as previously described [22].

236 The electrotrophic viability was assessed by a high-sensitivity flow cytometry
237 in the presence of the photocatalyst and light irradiation [7]. At the end of each
238 fed-batch operation, samples were collected from both the cathode electrode and from
239 the catholyte. Firstly, the electrotroph was split off by sonicating with a low specific
240 power of 9 J/mL (Bran-sonic CPXH Ultrasonifier). The mixed solution was
241 centrifuged and the electrotrophic pellets were re-suspended in a physiological saline
242 solution, which contained 50 ug/mL propidium iodide. After culturing for 15 minutes
243 at 37 °C in the dark, the cells were finally rinsed (twice), re-suspended in a normal

244 physiological saline solution and quantified by FD FACSCanto flow cytometer
245 (Bioscience).

246 The holes, H_2O_2 and radical species generated at the cathode were examined
247 using different trapping agents: 0.1 mM Fe(Ⅱ)-EDTA for H_2O_2, 0.5 mM sodium
248 oxalate for h^+, 0.5 mM isopropanol for $^{\bullet}OH$, and 2 mM p-benzoquinone for $O_2^{\bullet-}$.
249 These concentrations can sufficiently scavenge the photo-generated free radical while
250 negligibly affecting the activities of microorganisms and solution conductivity
251 [31-32].

252 The long-term stability of the Ag_3PO_4/g-C_3N_4 photocathodes was evaluated over
253 16 days operation of the reactors, with periodical supply of bicarbonate. In these
254 experiments, 3.0 ml of catholyte was sampled daily and an equal volume of 113.9 –
255 118.6 mM $NaHCO_3$ was replenished to maintain the initial concentration of inorganic
256 carbon at 23.8 mM each day. The controls were carried out by the above method,
257 except that the concentration of $NaHCO_3$ supplemented each day was different
258 (Ag_3PO_4: 80.0 – 87.0 mM; g-C_3N_4: 82.3 – 87.6 mM; bare graphite felt: 76.2 – 80.5
259 mM), to maintain the initial concentration at 23.8 mM.

260 The $CE_{acetate}$ and the residual hydrogen (CE_{H2}) were calculated according to Eqs.
261 1 – 2:

262 $$CE_{acetate} = \frac{8 \times n_a \times F}{\int_0^t I\,dt} \times 100\% \qquad (1)$$

263 $$CE_{H2} = \frac{2 \times n_b \times F}{\int_0^t I\,dt} \times 100\% \qquad (2)$$

264 where n_a (mol) is the mole amount of acetate, n_b (mol) is the mole amount of H_2, I (A)

is the current, F (96485 C/mole electron) is the Faraday constant and *t* is the operation time (s).

3 Results and discussion

3.1 Characterization of prepared photo-assisted cathode

The characteristic peaks in the XRD patterns of Ag_3PO_4 were consistent with the crystal planes of body-centered cubic Ag_3PO_4 (JCPDS 06-0505), exhibiting 20.96° (110), 29.76° (200), 33.36° (210), 36.64° (211), 47.84° (220), 52.76° (310), 55.12° (222), 57.34° (320), 61.72° (400) and 73.92° (322) (Fig. 1A) [20,33]. Those at 12.6° (100) and 27.4° (002) corresponded to g-C_3N_4 [34]. The Ag_3PO_4/g-C_3N_4 exhibited diffraction peaks corresponding to both Ag_3PO_4 and g-C_3N_4, confirming the successful combination of Ag_3PO_4 and g-C_3N_4. The absence of characteristic diffraction peak assigned to Ag nanoparticles excluded the photocorrosion phenomenon for the pristine Ag_3PO_4/g-C_3N_4, which was instead observed in other studies on photocatalytic reduction of CO_2 to CO and CH_4 [17].

Here Fig. 1

PL spectra characterized the separation efficiency of the photoinduced carriers. The maximum emission intensity of Ag_3PO_4/g-C_3N_4 was significantly weaker than that of g-C_3N_4 at the same wavelength of 455 nm (Fig. 1B), indicating strong interactions between Ag_3PO_4 and g-C_3N_4 and thus a much lower recombination rate of the photo-generated carriers.

The Ag_3PO_4/g-C_3N_4 cathode exhibited an order of magnitude higher

photocurrent than either Ag_3PO_4 or g-C_3N_4 (Fig. 1C), confirming a highly efficient charge carrier separation and transport in the Ag_3PO_4/g-C_3N_4 heterojunction. In the absence of electrotroph the photocurrent of the Ag_3PO_4/g-C_3N_4 cathode slightly increased (Fig. S2) due to the reduction of the electrotrophic photon absorption efficiency, however, the catalytic effect exerted by the electrotroph reduced the charge transfer resistance (R_{ct}) and was essential for the production of acetate from inorganic carbon. Similar behaviors have been observed with *Methanosarcina barkeri* on indium phosphide photocathode used for the production of methane [6], and with *Moorella thermoacetica* on cadmium sulfide (CdS) [2,5] or with *Serratia marcescens* on WO_3/MoO_3/g-C_3N_4 [7] used for the production of acetate from inorganic carbon.

UV-vis DRS spectra confirmed the optical absorption and band gaps of the photocatalysts (Fig. 1D). The considerable red-shift in the absorption edges of Ag_3PO_4/g-C_3N_4 (541 nm) and Ag_3PO_4 (526 nm) in comparison to g-C_3N_4 (454 nm) suggested that the Ag_3PO_4/g-C_3N_4 heterojunction utilizes a higher portion of the visible light spectrum to improve photocatalytic performance [20]. The band gaps (E_g) of g-C_3N_4 (2.73 eV) and Ag_3PO_4 (2.36 eV) were estimated by the Tauc plots (Fig. 1D) [35]. The positive slopes of the linear plots in the Mott-Schottky curves (Fig. S3) indicated that both g-C_3N_4 and Ag_3PO_4 were n-type semiconductors, while the conduction band edge potential (E_{CB}) of n-type semiconductor was usually 0.1 to 0.3 eV more negative than its flat-band potential (E_{FB}) [36]. Thus, the E_{CB} of g-C_3N_4 (-1.15 eV) and Ag_3PO_4 (0.25 eV) were calculated based on the E_{FB} for g-C_3N_4 and Ag_3PO_4 using the Mott-Schottky plots (Fig. S3). The valence band edge potentials

(E_{VB}) of g-C_3N_4 (1.58 eV) and Ag_3PO_4 (2.61 eV) were obtained according to the following formula $E_{VB} = E_{CB} + E_g$ [35]. The bands of the two semiconductors align to a potential Z-scheme mechanism.

The value of carrier density N_D for Ag_3PO_4/g-C_3N_4 (9.77×10^{17} cm^{-3}), calculated from the Mott-Schotty plots (Fig. S3), was significantly higher than the N_D of either Ag_3PO_4 (2.63×10^{17} cm^{-3}) or g-C_3N_4 (2.80×10^{17} cm^{-3}), indicating smaller charge transfer resistance and faster charge transfer in the heterojunction, thereby enhancing the photocatalytic process [37].

FTIR spectra were used to probe the chemical structure of the obtained samples (Fig. 1E). Pure Ag_3PO_4 represented two strong peaks at 542 and 943 cm^{-1}, which were assigned to the P-O stretching vibrations of PO_4^{3-}, while the strong characteristic peaks of g-C_3N_4 in the range 1200 − 1700 cm^{-1} corresponded to the typical stretching vibrations of the CN heterocycles [26]. The FTIR spectrum of Ag_3PO_4/g-C_3N_4 exhibited an overlap of the Ag_3PO_4 and g-C_3N_4 spectra, where the frequency of the two characteristic peaks of the Ag_3PO_4 phase, at 549 and 951 cm^{-1} in the Ag_3PO_4/g-C_3N_4 heterojunction, increased [26]. These results suggest structural interaction between the Ag_3PO_4 and g-C_3N_4 phases in the Ag_3PO_4/g-C_3N_4 heterojunction.

The absolute zeta potential values of Ag_3PO_4/g-C_3N_4 were invariably higher than those of g-C_3N_4 in the pH range from 4 to 12 (Fig. 1F), indicating improved dispersion of g-C_3N_4 through the introduction of Ag_3PO_4 [35]. In addition, the zeta potentials of Ag_3PO_4/g-C_3N_4 were always more negative than those of g-C_3N_4. The

more negative zeta potential of Ag_3PO_4/g-C_3N_4 and its improved dispersion, compared with the g-C_3N_4 consistently contributed to enhance the adsorption of the positively charged H^+ which favors a higher rate of H_2 production and in turn a high rate of acetate production through the Wood – Ljungdahl pathway in this system.

The visible C, N, O, Ag and P signals in the XPS spectra of Ag_3PO_4/g-C_3N_4 (Fig. 2A) confirmed its hybrid structure, consistent with the XRD results (Fig. 1A). The C 1s peak at 284.70 eV was attributed to C-C bonding of graphitic or amorphous carbons in Ag_3PO_4/g-C_3N_4 (Fig. 2B), whereas the other peak of C 1s at 287.28 eV was assigned to the C-$(N)_3$ in g-C_3N_4 [38]. The N 1s peak at 398.50 eV was assigned to sp^2-hybridization of N element (C=N-C) in Ag_3PO_4/g-C_3N_4 (Fig. 2C) whereas the peak at 399.52 eV belonged to amino functional groups having a hydrogen atom (C-N-H) and 401.04 eV ascribed to tertiary nitrogen (N-$(C)_3$) [26,38]. Regarding the Ag 3d spectrum in Ag_3PO_4/g-C_3N_4 (Fig. 2E), the two peaks at 367.82 (Ag $3d_{5/2}$) and 373.80 eV (Ag $3d_{3/2}$) were assigned to the Ag^+ of Ag_3PO_4 [20,33]. The binding energies at 530.55 and 531.68 eV were attributed to O 1s (Fig. 2D), whereas the peak at 530.55 eV was associated with the O_2 in Ag_3PO_4 and the peak at 531.68 eV ascribed to -OH groups on the surface of Ag_3PO_4/g-C_3N_4 [20]. The bond energy of P 2p of 132.91 eV was associated with the P^{5+} of Ag_3PO_4 (Fig. 2F) [20]. It is worth mentioning that the binding energies of C 1s and N 1s had slight negative shifts compared to g-C_3N_4, while the binding energies of Ag 3d, P 2p and O 1s exhibited slight red shifts compared to Ag_3PO_4. These results collectively indicated the strong interaction between g-C_3N_4 and Ag_3PO_4 due to π-backing bonding, similar to reports

353 with other photocatalysts [20,39].

354 **Here Fig. 2**

355 TEM images with different magnifications (Fig. 3) shows successful
356 immobilization of Ag_3PO_4 nanoparticles on the surface of g-C_3N_4 in Ag_3PO_4/g-C_3N_4
357 (Fig. 3A and B). The lattice fringe spacing of 0.265 nm in the Ag_3PO_4/g-C_3N_4 (Fig.
358 3B) was ascribed to the (210) crystal plane of Ag_3PO_4, exactly the same as that
359 observed in the pure Ag_3PO_4 sample (Fig. 3D) [40]. The presence and uniform
360 distribution of Ag, P, O, C and N elements in Ag_3PO_4/g-C_3N_4 was confirmed by the
361 element mapping results (Fig. S2B-F), further indicating successful integration of
362 Ag_3PO_4 and g-C_3N_4 into Ag_3PO_4/g-C_3N_4 heterostructures [40].

363 **Fig. 3**

364 The microstructures of the bare surface of the photocatalyst deposited on the
365 cathodes and in the presence of *S. marcescens* were observed by SEM. g-C_3N_4
366 showed a sheet structure (Fig. 4E and G) and uniform distribution on the graphite felt
367 (the inset of Fig. 4E), while Ag_3PO_4 nanoparticles formed more evident aggregates
368 (Fig. 4I and K). The Ag_3PO_4 particles uniformly dispersed on the surface of g-C_3N_4 in
369 the Ag_3PO_4/g-C_3N_4 (Fig. 4A and C). The density of electrotroph deposited on the
370 Ag_3PO_4/g-C_3N_4 and g-C_3N_4 electrodes was higher than on Ag_3PO_4 (Fig. 4C, G and K),
371 and this was ascribed to the excellent biocompatibility of g-C_3N_4 [13-14].

372 **Here Fig. 4**

373 Compared with the abiotic controls (Fig. 4B, F and J), the attached electrotroph
374 exhibited Na and K signals in EDS spectra, and the content of P increased accordingly

375 (Fig. 4D, H and L). The simultaneous presence of C, N, P, O and Ag signals in the
376 abiotic Ag_3PO_4/g-C_3N_4 cathode (Fig. 4B) indicated the successful assembling of the
377 g-C_3N_4 and Ag_3PO_4 in the composite.
378
379 *3.2 Optimization of operating parameters*
380 The ratio of Ag_3PO_4 and g-C_3N_4 of 1 : 2 achieved the highest rate of acetate
381 production (Fig. S4A), the optimal $CE_{acetate}$ (Fig. S4B), the most efficient separation
382 of electron-hole pairs (Fig. S4C), and the highest light response current (Fig. S4D).
383 Different Ag_3PO_4 and g-C_3N_4 ratios can form different electronic and structural
384 interactions in the Ag_3PO_4/g-C_3N_4 composite and thus influence the photocatalytic
385 performance as also observed in Z-scheme Ag_3PO_4/g-C_3N_4 composites used for
386 converting CO_2 to fuels [17]. The intensity of photoluminescence shown in Fig. S4C
387 is not only related to the separation efficiency of the charge carriers, but is also
388 affected by surface defects, oxygen vacancies and other properties of the measured
389 samples [41]. Thus, the photoluminescence results were expected to deviate from the
390 transient photocurrent response (Fig. S4D), which instead reflected more closely the
391 separation efficiency of the charge carriers [41].
392 The loading amount of Ag_3PO_4/g-C_3N_4 was optimized between the range 0.18 –
393 0.73 mg/cm^2 and reached an optimum at 0.41 mg/cm^2 in terms of acetate production,
394 $CE_{acetate}$ and photocurrent response (Fig. S5). Overloading of photocatalysts can
395 deactivate the activated molecules by collision with ground state molecules whereas
396 an appropriate loading of photocatalysts may avoid the unnecessary excess catalyst

and also ensure efficient absorption of light photons for efficient system performance, similar to other studies using TiO_2 [32]. Thus, a ratio of Ag_3PO_4 to g-C_3N_4 of 1 : 2 and a cathode photocatalyst loading of 0.41 mg/cm^2 were used in subsequent experiments.

3.3 MES performance

The Ag_3PO_4/g-C_3N_4 photocathode incorporating *S. marcescens* achieved an acetate production rate of 5.4 ± 0.1 mM/d (Fig. 5A) with a $CE_{acetate}$ of 93 ± 2% (Fig. 5D) and a residual hydrogen peroxide concentration of 35.5 ± 1.3 μM (Fig. 5C) with inorganic carbon consumption of 26 ± 1% (Fig. S6A) at a current density of 3.3 ± 0.1 A/m^2 (Fig. S6B). These were appreciably higher than the results obtained using a WO_3/MoO_3/g-C_3N_4 photocathode and *S. marcescens* under same experimental conditions (acetate: 3.1 ± 0.2 mM/d, $CE_{acetate}$: 73 ± 4%, inorganic carbon consumption: 20 ± 1%, current: 2.5 ± 0.3 A/m^2) [7]. These values were also higher than the production rates observed using CdS/gold nanoclusters and *Moorella thermoacetica* (0.1 − 0.5 mM/d), Si nanowire array/TiO_2/Ni and *Sporomusa ovata* (4.0 − 5.0 mM/d), or the abiotic AgCl/g-C_3N_4 (0.6 mM/d) under similar operational conditions (Table S1) [18,42-44]. The exceptionally high rate of acetate production reported using the abiotic TiO_2 nanotube/g-C_3N_4 system (Table S1) can be ascribed to the much higher photon flux emitted by the xenon lamp used (approximate 3.0-fold more than in this study) and to the short operational period of 1.0 h, although the long-term stability of the employed photocatalyst and product selectivity remained unexplored (Table S1) [45].

The performance was also significantly higher than the controls, under darkness

conditions (acetate: 2.7 ± 0.1 mM/d; $CE_{acetate}$: 67 ± 2%; inorganic carbon consumption: 21 ± 1%; current: 2.4 ± 0.1 A/m^2), or with either Ag_3PO_4 or g-C_3N_4 photocatalysts, in the presence or in the absence of light (Fig. 5A, D and Fig. S6). The poor performance recorded using the bare graphite felt cathode regardless of light irradiation (acetate: 1.6 ± 0.2 mM/d; $CE_{acetate}$: 61 ± 4%; inorganic carbon consumption: 14 ± 1%; current: 1.5 ± 0.1 A/m^2) highlighted the positive impact of combining the two semiconductors forming Ag_3PO_4/g-C_3N_4, which delivers in this system in a Z-scheme photocatalytic reaction mechanism as discussed in further sections. Moreover, the disappearance of acetate (Fig. 5A) and the lowest current (Fig. S6B) in the abiotic controls demonstrated the critical roles played by both *S. marcescens* species and Ag_3PO_4/g-C_3N_4 in this system. The impact of light irradiation was further evidenced by the significantly higher rates of H_2 production recorded with either the biotic or the abiotic Ag_3PO_4/g-C_3N_4 cathode in comparison to the values recorded under darkness (Fig. 5B). Thus, it may be inferred that the photo-generated electrons were used for H_2 production, in concert to the mechanism of H_2 evolution on g-C_3N_4 [12-15]. The trend of higher acetate production (Fig. 5A) corresponding to higher evolution of equivalent total H_2 (Fig. 5B), and lower concentration of residual H_2 (Fig. 5B), confirmed the function of H_2 as a mediator in the reduction of inorganic carbon through the Wood–Ljungdahl pathway [1].

Here Fig. 5

The photocorrosion of Ag_3PO_4/g-C_3N_4 was investigated by XRD (Fig. 5E) and XPS (Fig. 5F; Fig. S6C and D) analyses. Metallic silver in the catholyte was clearly

observed under OCCs, shown as four peaks (38.12°, 44.48°, 64.44°, 77.56°) (JCPDS No. 04-0783) [17,19,26], indicating that photocorrosion of Ag_3PO_4 was taking place. In contrast, under CCCs metallic Ag was not observed regardless of the presence or absence of *S. marcescens* or light. Similarly, in the high resolution Ag 3d spectrum of Ag_3PO_4/g-C_3N_4 (Fig. 5F), two pair peaks at 367.53/373.49 eV corresponding to metallic Ag and at 368.10/374.01 eV attributed to Ag^+ in Ag_3PO_4 [17,19-20,26] were observed under OCCs, while under CCCs these peaks were not observed regardless of the presence or absence of *S. marcescens* or light (Fig. 5F; Fig. S6C and D). These results collectively reflected the efficient inhibition of the photocorrosion process of Ag_3PO_4/g-C_3N_4 under CCCs. The photocorrosion was clearly prevented by the utilization of the H_2O_2 produced in-situ over the Ag_3PO_4/g-C_3N_4 cathode, since under CCCs the residual H_2O_2 (35.5 – 36.3 μM) was significantly lower than under OCCs (144 μM) regardless of the presence of *S. marcescens* (Fig. 5C). The absence of cathodic electrons under OCCs reasonably led to the none consumption and accumulation of H_2O_2, and the subsequent occurrence of photocorrosion of Ag_3PO_4 (Fig. 5F). Moreover, the absence of H_2O_2 in the controls in the absence of either light or photocatalyst under OCCs or CCCs, excluded the electrocatalytic production of H_2O_2. Considering the anaerobic conditions in the catholyte, the H_2O_2 was conclusively generated in-situ through the photocatalytic oxidation of water (Reactions 5 – 6) [46].

Flow cytometry is a high-sensitive approach to quantify the live/dead bacteria ratio in response to the changes in external environments [7]. The radical species

produced during the photocatalytic process had negligible detrimental impact on the total amount of *S. marcescens* supported on the Ag_3PO_4/g-C_3N_4 photocathodes, since the amount of inactive electrotroph varied negligibly: 4.7% under CCCs and light, compared to 4.4% in the absence of illumination, 3.8% using the bare graphite felt under illumination and 0.6% without propidium iodide staining (Fig. S7), consistent with the results obtained using the same electrotroph and WO_3/MoO_3/g-C_3N_4 photocathodes [7]. Similarly, negligible impact of the photocatalytic process has been observed in other photo-electrochemical processes, such as on the methane producer by *Methanosarcina barkeri* [6] or on the acetate producer by *Moorella thermoacetica* [2,5]. Quantification of the hydroxyl radicals by HPLC (0.8 μM) (Fig. S8) confirmed a significantly lower concentration than the harmful onset value reported for *Pseudomonas aeruginosa* of 3.0 μM [47], implying negligible impact of the hydroxyl radicals on the viability of *S. marcescens*. Moreover, the highest concentration of H_2O_2 produced in-situ (OCCs, 144 ± 3 μM, Fig. 5C) was appreciably lower than the detrimental concentrations reported for other bacteria such as *Xanthobacterflavus* sp. (4.5 mM) [48] or *Escherichia coli* (10 mM) [49]. Thus, potential detrimental effects of hydroxyl radicals and H_2O_2 on the viability of *S. marcescens* were excluded.

3.4 CV and EIS analysis

The reduction onset potential (E_{onset}) in the biotic Ag_3PO_4/g-C_3N_4 positively shifted to –0.30 V, compared to –0.33 V for the biotic Ag_3PO_4 and –0.35 V for the biotic g-C_3N_4 (Fig. 6A; Table S2). Meanwhile, the maximum reduction peak current

for Ag_3PO_4/g-C_3N_4 (Fig. 6A; Table S2) as well as its broadest peak in the first derivative CV (DCV) plots (Fig. 6B) collectively proved the efficient catalytic role of the Ag_3PO_4/g-C_3N_4 in the photo-assisted biocathodes. The more negative E_{onset} (–0.45 V) recorded with the bare graphite felt controls in the presence of *S. marcescens*, reflected the importance of combining both the photocatalyst and the electrotroph to achieve effective MES performance. Other studies using indium phosphide assembled with the *Methanosarcina barkeri* methane producer or CdS with the CO_2-reducing bacterium *Moorella thermoacetica* have reported similar conclusions [2,5-6].

Here Fig. 6

The EIS spectra (Fig. 6C and D) were analyzed by fitting spectra to an equivalent circuit (Fig. S9; Table S2). The presence of light irradiation invariably decreased the diffusion resistance (R_{dif}) and the charge transfer resistance (R_{ct}) in both the biotic (Fig. 6C; Table S2) and the abiotic (Fig. 6D; Table S2) cathodes, compared to the values observed in the absence of light irradiation. The value of R_{ct} was dominant over the electrolyte resistance (R_s) and the R_{dif}, and was significantly lower (30 Ω) than the controls without light irradiation (45 Ω), under abiotic conditions (59 Ω), with Ag_3PO_4 only (58 Ω), with g-C_3N_4 only (71 Ω) or with the bare graphite felt (79 Ω) (Fig. 6C and D; Table S2). The presence of the biofilm can change the conditions surrounding the electrode material, and thus the electron transfer mechanisms on the biotic and the abiotic electrodes may not the same [50]. The lower R_{ct} recorded under biotic photo-assisted conditions was attributed to the *S. marcescens* biofilm creating a higher proportion of potential active sites on the cathode surface

favoring charge transfer reactions. Such effect has also been observed in anodic pure or mixed exoelectrogens in the absence of light irradiation [50]. These results clearly highlighted the impact of light irradiation on the activation of Ag_3PO_4/g-C_3N_4 hybrid photocatalyst, which in turn reduced the internal resistance to electron transfer favoring the bio-transformation of inorganic carbon to acetate (Fig. 5A) with enhanced circuital current (Fig. S6B).

3.5 Photocatalytic mechanism over Ag_3PO_4/g-C_3N_4

ESR analysis was performed to detect oxygen-containing radicals formed in the MES (Fig. 7A-B). DMPO-$^{\bullet}$OH signals (four characteristic peaks, 1:2:2:1) were clearly observed for the biotic Ag_3PO_4/g-C_3N_4 cathode under light irradiation, while no signals were detected in the absence of light irradiation. The signals strength in both biotic and abiotic Ag_3PO_4/g-C_3N_4 cases were of equivalent amplitude and both were appreciably lower than the signal recorded with the biotic Ag_3PO_4/g-C_3N_4 under OCC (Fig. 7A) as expected. Moreover, no DMPO-$O_2^{\bullet-}$ signals were observed under the same conditions, excluding the presence of $O_2^{\bullet-}$ in the MES (Fig. 7B). Thus, it was clearly demonstrated the photocatalytic generation of $^{\bullet}$OH formed from water oxidation over the irradiated Ag_3PO_4/g-C_3N_4 heterojunction, with the amount of $^{\bullet}$OH consistent with the residual amount of H_2O_2 formed after fast recombination of $^{\bullet}$OH (Fig. 5C). A similar pattern has been observed in other studies using Ag_3PO_4/g-C_3N_4 or g-C_3N_4 photocatalysts [16,26,29].

The predominant photocatalytic mechanisms over Ag_3PO_4/g-C_3N_4 were further

investigated through active species trapping experiments to determine the main reactive radical species in the system. In the presence of trapping agents such as Fe(II)-EDTA, isopropanol or sodium oxalate, the acetate production (–28 ± 2%) (Fig. 7C), the current density (–17 ± 1%) and the $CE_{acetate}$ (–13 ± 2%) (Fig. 7D) decreased by equal amounts, reflecting the positive impact of H_2O_2 on this system performance. Since H_2O_2 was not detected in these anaerobic trapping reactions (Fig. 7C), the in-situ production of H_2O_2 can be attributed to the fast recombination of hydroxyl radicals formed by water oxidation by the photogenerated holes (Reactions 5 – 6), which was further supported by the decreased current in the presence of the scavengers. The addition of the $^{\bullet}OH$ scavenger, isopropanol, resulted in complete disappearance of H_2O_2 (formed by fast $^{\bullet}OH$ recombination) (Fig. 7C), confirming the existence of $^{\bullet}OH$ in this MES, in agreement with the ESR results (Fig. 7A). The $O_2^{\bullet-}$ scavenger *p*-benzoquinone negligibly affected system performance (Fig. 7C), indicating that $O_2^{\bullet-}$ was not a radical species present in the system, as also shown by the ESR results (Fig. 7B). The anaerobic conditions in the catholyte also excluded the possibility of forming $O_2^{\bullet-}$. These results and the position of the band levels of the semiconductors suggest a Z-scheme photocatalytic mechanism for the anaerobic Ag_3PO_4/g-C_3N_4 photocathode MES system (Fig. 8). Under visible light irradiation, g-C_3N_4 and Ag_3PO_4 were induced to generate electron-hole charge pairs. The photo-induced electrons were excited from the VB to the corresponding CB, whereas the photo-generated electrons were injected from the CB of Ag_3PO_4 into the VB of g-C_3N_4, thereby suppressing the recombination of charge carriers in the same material.

552 The accumulated reductive electrons in the CB of the g-C_3N_4 were utilized for the
553 evolution of H_2, whereas the more oxidative holes in the VB of the Ag_3PO_4 strongly
554 oxidized water to produce H_2O_2 in-situ. The proximity between the electron-donor
555 cathode and the electron-acceptor H_2O_2 formed a driving force, in which the H_2O_2
556 produced in-situ around the Ag_3PO_4/g-C_3N_4 photocathode was preferentially reduced
557 to water, protecting the photocorrosion of Ag_3PO_4, based on the appreciable higher
558 redox potential (Reactions 1 – 2). In parallel, the hydrogen evolving on g-C_3N_4 was
559 favorably metabolized by *S. marcescens* with HCO_3^- to produce acetate through the
560 Wood-Ljungdahl pathway [1]. Such mechanism successfully prevented the
561 photo-etching of Ag(I) and thus the superior photocatalytic performance of the
562 Ag_3PO_4/g-C_3N_4 photocathode.

563 **Here Fig. 7**

564 **Here Fig. 8**

565

566 *3.6 MES performance as a function of operational time*

567 Acetate production (Fig. 9A) and $CE_{acetate}$ (Fig. 9B) were negligibly affected at a
568 prolonged operational time of 1.0 d and decreased thereafter, due to the progressive
569 reduction of the concentration of HCO_3^- in the system (Fig. 9C), while the amount of
570 residual H_2O_2 produced in-situ (34.6-35.5 μM) (Fig. 9D) and the circuital current (Fig.
571 S10) did not vary. These values were always higher than those in the controls using
572 g-C_3N_4 only, Ag_3PO_4 only, or bare graphite felt only cathodes (Fig. 9; Fig. S10),
573 confirming the photocatalytic Z-scheme mechanism over the Ag_3PO_4/g-C_3N_4
574 electrode.

Here Fig. 9

EIS analysis (Fig. 9E and F) show the dominant role and sharp increase of the diffusional resistance R_{dif} from 34 Ω at 0.5th day to 90 Ω at 1st day and the further sharp climb to 1830 Ω at 2nd day, compared to a very slight increase of R_s and R_{ct} (Table S3). This phenomenon resulted from the progressive depletion of HCO_3^- in the semi-batch system, until insufficient supply of HCO_3^- decreased the diffusion rate of reactant and thus R_{dif} reached extremely high values. A similar behavior has been reported in other studies on the production of acetate performed with the hybrid of CdS and *Moorella thermoacetica* [5] under an inadequate supply of CO_2. Thus, bicarbonate was subsequently added after 1.0 day operation to sustain high rates of acetate production over prolonged continuous operation of the MES up to 16 days.

3.7 MES performance with periodical addition of bicarbonate

Prolonged operation of the MES cell up to 16 days with periodical addition of bicarbonate increased the acetate production linearly, accumulating up to 81.0 ± 0.2 mM of acetate (Fig. 10A) with a reasonably flat $CE_{acetate}$ of 89 ± 1% (Fig. 10B) and a regular change of bicarbonate (Fig. 10C) at 16th days operation, appreciably higher than the results with the bare graphite felt cathode. The average acetate production rate of 5.03 ± 0.01 mM/d was 3.06, 2.84 and 3.26 times higher than the rates observed with the Ag_3PO_4 only, the g-C_3N_4 only or the bare graphite felt only cathodes, respectively (Fig. 10A). The acetate production rate was higher than the reported 2.83 ± 0.01 mM/d by mixed culture on a 3D reduced graphene oxide modified carbon felt

cathode with continuous CO_2 sparging in the absence of light irradiation [51] at similar operational periods. Residual H_2 was reasonably lower than the values in the controls using Ag_3PO_4 only, g-C_3N_4 only or bare graphite felt only cathodes (Fig. S11A), consistent with the higher rate of acetate production in Fig. 10A.

Here Fig. 10

Ag leaching was sharply accumulated from 1.1 ± 0.1% at the 1st day to 3.0 ± 0.1% at the 4th day and stabilized at 3.9 ± 0.2% after the 7th day (Fig. S11B). EIS analysis demonstrated the stable (99 – 102 Ω) and dominant role of R_{dif} over a slight increase observed in the R_{ct} (from 35 Ω to 41 Ω) and the steady value of R_s (4.0 – 4.2 Ω) during the entire 16 days operation (Fig. S11C and D; Table S4). This R_{dif} was appreciably lower than the 1019 – 1830 Ω at 1.5 – 2.0 days without periodical supply of bicarbonate (Table S3), confirming the necessity of periodical supply of bicarbonate to achieve lower R_{dif} and thus high levels of acetate production.

Metallic Ag was none detected in the XRD (Fig. 10E) or XPS (Fig. 10F) spectra in addition to the absence of peak splitting in the Ag 3d spectrum, clearly demonstrating the appreciable inhibition of the photocorrosion of Ag_3PO_4 over an uninterrupted operational cycle. The residual concentration of H_2O_2 was stable in the range of 33.7 – 35.7 μM (Fig. 10D), similar to the values observed under fed-batch operation (Fig. 5C) implying negligible detrimental effects on the viability of the *S. marcescens*, also shown by flow cytometry (Fig. S7). The concentration of H_2O_2 was significantly lower than the threshold values (4.5 – 10 mM) reported for conventional bacteria such as *Xanthobacterflavus* sp. or *Escherichia coli* [48-49].

SEM-EDS analysis of the Ag_3PO_4/g-C_3N_4 biocathode after 16 days operation (Fig. S12) demonstrated similar particle size and morphology as those observed after a short operational period of 0.5 d (Fig. 4). Considering the slight increase in internal resistance (Fig. S11C and D), these results clearly confirmed the stability of the Ag_3PO_4/g-C_3N_4 photo-assisted biocathode and the in-situ utilization of H_2O_2 for the inhibition of Ag_3PO_4 photocorrosion.

The emerging field of bio-electro-photocatalysis for the reduction of inorganic carbon via hydrogen mediation, represents a largely unexplored line of investigation [18]. While effective cathodic materials with appropriate hydrogen catalytic activity at near-neutral pH need to be selected, the assessment of the intracellular complex reactions driven by the cathodic photocatalytic materials remain unexplored. Electrotrophs physiologically respond to changes of the external environment (e.g., circuital current, heavy metals, pH) by releasing extracellular polymeric substances (EPS) and by regulating the activity of intracellular enzymes [8,52-55]. Thus, under light irradiation and as a response to the H_2O_2 produced in-situ, the locally anaerobic micro-environment created by the EPS released by the *S. marcescens* and the changes of its typical intracellular enzymatic activities, might have allowed for the efficient system performance and long-term stability. The identification of the associated genetic regulating networks in *S. marcescens* is also necessary to achieve further increase in the acetate yield.

4. Conclusions

In summary, a Ag_3PO_4/g-C_3N_4 cathode with excellent photocatalytic activity was successfully applied in a MESs incorporating *S. marcescens* Q1 for efficient acetate production from inorganic carbon. The in-situ produced H_2O_2 through the anaerobic photocatalytic oxidation of water, was simultaneously utilized for effective suppression of the photocorrosion of Ag_3PO_4 and this was crucial for improving the stability of the Ag_3PO_4/g-C_3N_4 photocathode. The photoinduced electrons on the conduction band of Ag_3PO_4/g-C_3N_4 were used for the evolution of H_2 and subsequent metabolism by *S. marcescens* Q1 with supplemented HCO_3^- for acetate production. Acetate accumulated up to 81.0 ± 0.2 mM with a $CE_{acetate}$ of 89 ± 1% over a 16 days with daily feed of bicarbonate. This study provides a sustainable and feasible strategy for inhibiting the photocorrosion of Ag_3PO_4 in Ag_3PO_4/g-C_3N_4 hybrid photocatalysts, thus achieving efficient acetate production from inorganic carbon in the photo-assisted MESs biocathodes.

Conflicts of interest

There are no conflicts to declare.

Acknowledgements

The authors gratefully acknowledge financial support from the National Natural Science Foundation of China (Nos. 21777017 and 52070032).

References

[1] E. Blanchet, F. Duquenne, Y. Rafrafi, L. Etcheverry, B. Erable, A. Bergel, Importance of the hydrogen route in up-scaling electrosynthesis for microbial CO_2 reduction, Energy Environ. Sci. 8 (2015) 3731–3744. DOI: 10.1039/C5TA05503B

[2] K.K. Sakimoto, A.B. Wong, P. Yang, Self-photosensitization of nonphotosynthetic bacteria for solar-to-chemical production, Science. 351 (2016) 74–77. DOI:

10.1126/science.aad3317
[3] Y. Jiang, R.J. Zeng, Expanding the product spectrum of value added chemicals in microbial electrosynthesis through integrated process design - a review, Bioresour. Technol. 269 (2018) 503–512. DOI: 10.1016/j.biortech.2018.08.101
[4] Y. Jiang, H.D. May, L. Lu, P. Liang, X. Huang, J.Z. Ren, Carbon dioxide and organic waste valorization by microbial electrosynthesis and electro-fermentation, Water Res. 149 (2019) 42–55. DOI: 10.1016/j.watres.2018.10.092
[5] K.K. Sakimoto, S.J. Zhang, P.D. Yang, Cysteine-cystine photoregeneration for oxygenic photosynthesis of acetic acid from CO_2 by a tandem inorganic-biological hybrid system, Nano Lett. 16 (2016b) 5883–5887. DOI: 10.1021/acs.nanolett.6b02740
[6] E.M. Nichols, J.J. Gallagher, C. Liu, Y. Su, J. Resasco, Y. Yu, Y. Sun, P. Yang, M.C.Y. Chang, C.J. Chang, Hybrid bioinorganic approach to solar-to-chemical conversion, Proc, Natl. Acad. Sci. USA. 112 (2015) 11461–11466. DOI: 10.1073/pnas.1508075112
[7] Z. Cai, L. Huang, X. Quan, Z. Zhao, Y. Shi, G. Li Puma, Acetate production from inorganic carbon (HCO_3^-) in photo-assisted biocathode microbial electrosynthesis systems using WO_3/MoO_3/g-C_3N_4 heterojunctions and *Serratia marcescens* species, Appl. Catal. B-Environ. 267 (2020) 118611. DOI: 10.1016/j.apcatb.2020.118611
[8] Z.G. Yi, J.H. Ye, N. Kikugawa, T. Kako, S.X. Ouyang, H. Stuart-Williams, H. Yang, J.Y. Cao, W.J. Luo, Z.S. Li, An orthophosphate semiconductor with photooxidation properties under visible-light irradiation, Nat. Mater. 9 (2010) 559–564. DOI: 10.1038/nmat2780
[9] Y.P. Bi, S.X. Ouyang, N. Umezawa, J.Y. Cao, J.H. Ye, Facet effect of single-crystalline Ag_3PO_4 sub-microcrystals on photocatalytic properties, J. Am. Chem. Soc. 133 (2011) 6490–6492. DOI: 10.1021/ja2002132
[10] N. Umezawa, O.Y. Shuxin, J.H. Ye, Theoretical study of high photocatalytic performance of Ag_3PO_4, Phys. Rev. B. 83 (2011) 035202. DOI: 10.1103/PhysRevB.83.035202
[11] D.J. Martin, G.G. Liu, S.J.A. Moniz, Y,P, Bi, A.M. Beale, J.H. Ye, J.W. Tang, Efficient visible driven photocatalyst, silver phosphate: performance, understanding and perspective, Chem. Soc. Rev. 44 (2015) 7808–7828. DOI: 10.1039/C5CS00380F
[12] J. Fu, Q. Xu, J. Low, C. Jiang, J. Yu, Ultrathin 2D/2D WO_3/g-C_3N_4 step-scheme H_2-production photocatalyst, Appl. Catal. B-Environ. 243 (2019) 556–565. DOI: 10.1016/j.apcatb.2018.11.011
[13] Y. Li, L. Ding, Y. Guo, Z. Liang, H. Cui, J. Tian, Boosting the photocatalytic ability of g-C_3N_4 for hydrogen production by Ti_3C_2 MXene quantum dots, ACS Appl. Mater. Interfaces 11 (2019) 41440−41447. DOI: 10.1021/acsami.9b14985
[14] J. Jiang, X. Wang, Y. Liu, Y. Ma, T. Li, Y. Lin, T. Xie, S. Dong, Photo-fenton degradation of emerging pollutants over Fe-POM nanoparticle/porous and ultrathin g-C_3N_4 nanosheet with rich nitrogen defect: Degradation mechenism, pathways, and products toxicity assessment, Appl. Catal. B-Environ. 278 (2020) 119349. DOI: 10.1016/j.apcatb.2020.119349

[15] J. Jiang, X. Wang, C. Zhang, T. Li, Y. Lin, T. Xie, S. Dong, Porous 0D/3D $NiCo_2O_4$/g-C_3N_4 accelerate emerging pollutant degradation in PMS/vis system: Degradation mechanism, pathway and toxicity assessment, Chem. Eng. J. 397 (2020) 125356. DOI: 10.1016/j.cej.2020.125356

[16] X. Yang, L. Tian, X. Zhao, H. Tang, Q. Liu, G. Li, Interfacial optimization of g-C_3N_4-based Z-scheme heterojunction toward synergistic enhancement of solar-driven photocatalytic oxygen evolution, Appl. Catal. B-Environ. 244 (2019) 240–249. DOI: 10.1016/j.apcatb.2018.11.056

[17] Y. He, L. Zhang, B. Teng, M. Fan, New application of Z-Scheme Ag_3PO_4/g-C_3N_4 composite in converting CO_2 to fuel, Environ. Sci. Technol. 49 (2015) 649–656. DOI: 10.1021/es5046309

[18] S. Cestellos-Blanco, H. Zhang, J.M. Kim, Y. Shen, P. Yang, Photosynthetic semiconductor biohybrids for solar-driven biocatalysis, Nat. Catal. 3 (2020) 245–255. DOI: 10.1038/s41929-020-0428-y

[19] T. Cai, L. Wang, Y. Liu, S. Zhang, W. Dong, H. Chen, X. Yi, J. Yuan, X. Xia, C. Liu, S. Luo, Ag_3PO_4/Ti_3C_2 MXene in terface materials as a Schottky catalyst with enhanced photocatalytic activities and anti-photocorrosion performance, Appl. Catal. B-Environ. 263 (2018) 545–554. DOI: 10.1016/j.apcatb.2018.08.053

[20] C. Liang, L. Zhang, H. Guo, C. Niu, X. Wen, N. Tang, H. Liu, Y. Yang, B. Shao, G. Zeng, Photo-removal of 2,2′4,4′-tetrabromodiphenyl ether in liquid medium by reduced graphene oxide bridged artificial Z-scheme system of Ag@Ag_3PO_4/g-C_3N_4, Chem. Eng. J. 361 (2019) 373–386. DOI: 10.1016/j.cej.2018.12.092

[21] J. Jia, W. Huang, C. Feng, Z. Zhang, K. Zuojiao, J. Liu, C. Jiang, Y. Wang, Fabrication of g-C_3N_4/Ag_3PO_4-H_2O_2 heterojunction system with enhanced visible-light photocatalytic activity and mechanism insight, J. Alloys Compd. 790 (2019) 616–625. DOI: 10.1016/j.jallcom.2019.03.238

[22] Q. Wang, L. Huang, X. Quan, Q. Zhao, Preferable utilization of in-situ produced H_2O_2 rather than externally added for efficient deposition of tungsten and molybdenum in microbial fuel cells, Electrochim. Acta. 247 (2017) 880–890. DOI: 10.1016/j.electacta.2017.07.079

[23] R. Cai, Y. Kubota, A. Fujishima, Effect of copper ions on the formation of hydrogen peroxide from photocatalytic titanium dioxide particles, J. Catal. 219 (2003) 214–218. DOI: 10.1016/S0021-9517(03)00197-0

[24] K. Fuku, K. Sayama, Efficient oxidative hydrogen peroxide production and accumulation in photoelectrochemical water splitting using a tungsten trioxide/bismuth vanadate photoanode, Chem. Commun. 52 (2016) 5406–5409. DOI: 10.1039/C6CC01605G

[25] Y. Zhao, Y. Liu, J. Cao, H. Wang, M. Shao, H. Huang, Y. Liu, Z. Kang, Efficient production of H_2O_2 via two-channel pathway over ZIF-8/C_3N_4 composite photocatalyst without any sacrificial agent, Appl. Catal. B-Environ. 278 (2020) 119289. DOI: 10.1016/j.apcatb.2020.119248

[26] J. Zhang, J. Lv, K. Dai, C. Liang, J. Zhu, Facile and green synthesis of novel porous g-C_3N_4/Ag_3PO_4 composite with enhanced visible light photocatalysis, Ceram. Int. 43 (2017) 1522–1529. DOI: 10.1016/j.ceramint.2016.10.125

[27] Q. Wang, L. Huang, X. Quan, G. Li-Puma, Sequential anaerobic and electro-Fenton processes mediated by W and Mo oxides for degradation/mineralization of azo dye methyl orange in photo assisted microbial fuel cells, Appl. Catal. B-Environ. 245 (2019) 672–680. DOI: 10.1016/j.apcatb.2019.01.026

[28] Q. Wang, Z. Cai, L. Huang, Y. Pan, X. Quan, G. Li-Puma, Intensified degradation and mineralization of antibiotic metronidazole in photo-assisted microbial fuel cells with Mo-W catalytic cathodes under anaerobic or aerobic conditions in the presence of Fe(III), Chem. Eng. J. 376 (2019) 119566. DOI: 10.1016/j.cej.2018.07.168

[29] C. Zhao, Z. Chen, J. Xu, Q. Liu, H. Xu, H. Tang, G. Li, Y. Jiang, F. Qu, Z. Lin, X. Yang, Probing supramolecular assembly and charge carrier dynamics toward enhanced photocatalytic hydrogen evolution in 2D graphitic carbon nitride nanosheets, Appl. Catal. B-Environ. 256 (2019) 117867. DOI: 10.1016/j.apcatb.2019.117867

[30] L. Huang, B. Yao, D. Wu, X. Quan, Complete cobalt recovery from lithium cobalt oxide in self-driven microbial fuel cell e Microbial electrolysis cell systems, J. Power Sources 259 (2014) 54–64. DOI: 10.1016/j.jpowsour.2014.02.061

[31] Y. Chen, T.W. Ng, A. Lu, Y. Li, H.Y. Yip, T. An, G. Li, H. Zhao, M. Gao, P. Wong, Comparative study of visible-light-driven photocatalytic inactivation of two different wastewater bacteria by natural sphalerite, Chem. Eng. J. 234 (2013) 43–48. DOI: 10.1016/j.cej.2013.08.106

[32] Z. Zhao, W. Zhang, X. Lv, Y. Sun, F. Dong, Y. Zhang, Noble metal-free Bi nanoparticles supported on TiO_2 with plasmon-enhanced visible light photocatalytic air purification, Environ. Sci.: Nano. 3 (2016) 1306–1317. DOI: 10.1039/C6EN00341A

[33] Q. Xiang, D. Lang, T. Shen, F. Liu, Graphene-modified nanosized Ag_3PO_4 photocatalysts for enhanced visible-light photocatalytic activity and stability, Appl. Catal. B-Environ. 162 (2015) 196–203. DOI: 10.1016/j.apcatb.2014.06.051

[34] H. Gao, R. Cao, X. Xu, S. Zhang, Y. Huang, H. Yang, X. Deng, J. Li, Construction of dual defect mediated Z-scheme photocatalysts for enhanced photocatalytic hydrogen evolution, Appl. Catal. B-Environ. 245 (2019) 399–409. DOI: 10.1016/j.apcatb.2019.01.004

[35] X. Yang, L. Tian, X. Zhao, H. Tang, Q. Liu, G. Li, Interfacial optimization of g-C_3N_4-based Z-scheme heterojunction toward synergistic enhancement of solar-driven photocatalytic oxygen evolution, Appl. Catal. B-Environ. 244 (2019) 240–249. DOI: 10.1016/j.apcatb.2018.11.056

[36] F. Meng, J. Li, S.K. Cushing, M. Zhi, N. Wu, Solar hydrogen generation by nanoscale p–n junction of p-type molybdenum disulfide/n-type nitrogen-doped reduced graphene oxide, J. Am. Chem. Soc. 135 (2013) 10286–10289. DOI: 10.1021/ja404851s

[37] H.S. Park, K.E. Kweon, H. Ye, E. Paek, G.S.Hwang, A.J. Bard, Factors in the metal doping of $BiVO_4$ for improved photoelectrocatalytic activity as studied by

798 scanning electrochemical microscopy and first-principles density-functional
799 calculation, J. Phys. Chem. C. 115 (2011) 17870–17879. DOI: 10.1021/jp204492r
800 [38] Z. Lan, G. Zhang, X. Wang, A facile synthesis of Br-modified g-C_3N_4
801 semiconductors for photoredox water splitting, Appl. Catal. B-Environ. 192 (2016)
802 116–125. DOI: 10.1016/j.apcatb.2016.03.062
803 [39] W. Yu, D. Xu, T. Peng, Enhanced photocatalytic activity of g-C_3N_4 for selective
804 CO_2 reduction to CH_3OH via facile coupling of ZnO: a direct Z-scheme mechanism,
805 J. Mater. Chem. A. 3 (2015) 19936–19947. DOI: 10.1039/C5TA05503B
806 [40] P. Zhu, Y. Chen, M. Duan, M. Liu, P. Zou, Structure and properties of
807 Ag_3PO_4/diatomite photocatalysts for the degradation of organic dyes under visible
808 light irradiation, Powder Technol. 336 (2018) 3193–3202. DOI:
809 10.1016/j.powtec.2018.05.060
810 [41] A. Galdamez-Martinez, G. Santana, F. Guell, PR. Martinez-Alanis, A. Dutt,
811 Photoluminescence of ZnO nanowires: A review, Nanomaterials. 10 (2020) 857.
812 DOI: 10.3390/nano10050857
813 [42] C. Liu, J.J. Gallagher, K.K. Sakimoto, E.M. Nichols, C. J. Chang, M.C.Y. Chang,
814 P. Yang, Nanowire-bacteria hybrids for unassisted solar carbon dioxide fixation to
815 value-added chemicals, Nano Lett. 15 (2015) 3634–3639. DOI:
816 10.1021/acs.nanolett.5b01254
817 [43] Z. Ji, H. Zhang, H. Liu, O.M. Yaghi, P. Yang, Cytoprotective metal-organic
818 frameworks for anaerobic bacteria, Proc, Natl. Acad. Sci. USA. 115 (2018)
819 10582–10587. DOI: 10.1073/pnas.1808829115
820 [44] Y. Su, S. Cestellos-Blanco, J. M. Kim, Y. Shen, Q. Kong, D. Lu, C. Liu, H.
821 Zhang, Y. Cao, P. Yang, Close-packed nanowire-bacteria hybrids for efficient
822 solar-driven CO_2 fixation, Joule. 4 (2020) 800–811. DOI:
823 10.1016/j.joule.2020.03.001
824 [45] J. Wu, Y. Feng, D. Li, X. Han, J. Liu, Efficient photocatalytic CO_2 reduction by
825 P-O linked g-C_3N_4/TiO_2 nanotubes Z-scheme composites, Energy 178 (2019)
826 168−175. DOI: 10.1016/j.energy.2019.04.168
827 [46] X.J. Shi, S. Siahrostami, G.L. Li, Y.R. Zhang, P. Chakthranont, F. Studt, T.F.
828 Jaramillo, X.L. Zheng, J.K. Norskov, Understanding activity trends in
829 electrochemical water oxidation to form hydrogen peroxide, Nat. Commun. 8 (2017)
830 701. DOI: 10.1038/s41467-017-00585-6
831 [47] B. Stenuit, L. Eyers, R. Rozenberg, J.L. Habib-Jiwan, S. Matthijs, P. Cornelis,
832 S.N. Agathos, Denitration of 2,4,6-trinitrotoluene in aqueous solutions using
833 small-molecular-weight catalyst(s) secreted by *Pseudomonas aeruginosa* ESA-5,
834 Environ. Sci. Technol. 43 (2009) 2011–2017. DOI: 10.1021/es8024319
835 [48] J. Howsawkeng, R.J. Watts, D.L.Washington, A.L. Teel, T.F. Hess, R.L.
836 Crawford, Evidence for simultaneous abiotic-biotic oxidations in a
837 microbial-Fenton's system, Environ. Sci. Technol. 35 (2001) 2961–2966. DOI:
838 10.1021/es001802x
839 [49] B. Demple, J. Halbrook, Inducible repair of oxidative DNA damage in
840 *Escherichia coli*, Nature. 304 (1983) 466–468. DOI: 10.1038/304466a0
841 [50] Z. He, F. Mansfeld, Exploring the use of electrochemical impedance

spectroscopy (EIS) in microbial fuel cell studies, Energy Environ. Sci. 2 (2019) 215–219. DOI: 10.1039/B814914C

[51] G. Mohanakrishna, K. Vanbroekhoven, D. Pant, Impact of dissolved carbon dioxide concentration on the process parameters during its conversion to acetate through microbial electrosynthesis, React. Chem. Eng. 3 (2018) 371–378. DOI: 10.1039/C7RE00220C

[52] X. Hou, L. Huang, P. Zhou, F. Tian, Y. Tao, G. Li Puma, Electrosynthesis of acetate from inorganic carbon (HCO_3^-) with simultaneous hydrogen production and Cd(II) removal in multifunctional microbial electrosynthesis systems (MES), J. Hazard. Mater. 371 (2019) 463–473. DOI: 10.1016/j.jhazmat.2019.03.028

[53] X. Hou and L. Huang, Synergetic magnetic field and loaded Fe3O4 for simultaneous efficient acetate production and Cr(VI) removal in microbial electrosynthesis systems, Chem. Eng. J. Adv. 2 (2020) 100019. DOI: 10.1016/j.ceja.2020.100019

[54] J. Hou, L. Huang, P. Zhou, Y. Qian, N. Li, Understanding the interdependence of strain of electrotroph, cathode potential and initial Cu(II) concentration for simultaneous Cu(II) removal and acetate production in microbial electrosynthesis systems, Chemosphere 243 (2020) 125317. DOI: 10.1016/j.chemosphere.2019.125317

[55] H. Yu, Molecular insights into extracellular polymeric substances in activated sludge, Environ. Sci. Technol. 54 (2020) 7742–7750. DOI: 10.1021/acs.est.0c00850

886

887 **Figure captions**

888 **Fig. 1** XRD patterns (A), photoluminescence spectra (B), biotic transient photocurrent
889 responses (C), UV – vis DRS spectra (D), FTIR spectra (E) and Zeta potential (F) of
890 the cathodes with or without (control) g-C_3N_4 or/and Ag_3PO_4 deposits.

891 **Fig. 2** XPS spectra of survey spectra of (A) g-C_3N_4, Ag_3PO_4 and Ag_3PO_4/g-C_3N_4, and
892 high resolution spectra of C 1s (B), N 1s (C), O 1s (D), Ag 3d (E) and P 2p (F) for
893 g-C_3N_4, Ag_3PO_4 or Ag_3PO_4/g-C_3N_4.

894 **Fig. 3** TEM images of Ag_3PO_4/g-C_3N_4 (A and B), Ag_3PO_4 only (C and D), and g-C_3N_4
895 only (E and F) with different magnifications.

896 **Fig. 4** SEM images on electrodes of Ag_3PO_4/g-C_3N_4 (A and C), g-C_3N_4 only (E and
897 G), and Ag_3PO_4 only (I and K) without (A, E and I) or with (C, G and K) *S.*
898 *marcescens*. EDS spectra on the sites of either no coverage (B, F and J) or coverage
899 (D, H, and L) of *S. marcescens* on electrodes of Ag_3PO_4/g-C_3N_4 (B and D), g-C_3N_4
900 only (F and H) and Ag_3PO_4 only (J and L) (Operational time: 0.5 d).

901 **Fig. 5** Comparison of acetate (A) and hydrogen (B) production, residual hydrogen
902 peroxide (C) and coulombic efficiency for acetate production ($CE_{acetate}$) (D), XRD
903 patterns (E) and high-resolution spectra of Ag 3d (F) of Ag_3PO_4/g-C_3N_4 under various
904 conditions (operation time: 0.5 d).

905 **Fig. 6** CVs (A) and DCVs (B) of the *S. marcescens* attached cathodes with or without
906 (control) g-C_3N_4 or/and Ag_3PO_4 loads in the presence or absence (control) of
907 illumination. Nyquist plots of EIS analysis of biotic (C) or abiotic (D) cathodes
908 (operational time: 0.5 d).

909 **Fig. 7** ESR spectra of the DMPO-$^{\cdot}$OH (A) and DMPO-$O_2^{\cdot-}$ (B) adducts recorded with

910 different conditions for Ag_3PO_4/g-C_3N_4. Comparison of acetate and H_2O_2 production
911 (C), and current density and $CE_{acetate}$ (D) in the presence or absence of different
912 trapping agents (operational time: 0.5 d).

913 **Fig. 8** Schematic diagram of the Ag_3PO_4/g-C_3N_4 photocathode in the photo-assisted
914 biocathode MES.

915 **Fig. 9** Time course of acetate production (A), $CE_{acetate}$ (B), inorganic carbon
916 consumption (C), residual H_2O_2 (D), and Nyquist plots of EIS spectra (E and F) of the
917 cathodes with Ag_3PO_4/g-C_3N_4 or bare graphite felt (E), or g-C_3N_4 or Ag_3PO_4 (F)
918 (operational time: 2.0 d).

919 **Fig. 10** Acetate production (A), $CE_{acetate}$ (B), residual inorganic carbon consumption
920 (C), residual H_2O_2 (D) with periodical addition of bicarbonate (Black arrows in A – D
921 indicated the points of bicarbonate addition). XRD (E) and XPS (F) of
922 Ag_3PO_4/g-C_3N_4 at the end of a 16 d operation with periodical addition of bicarbonate.

Figure 1

Click here to access/download;Figure;Fig. 1.tif

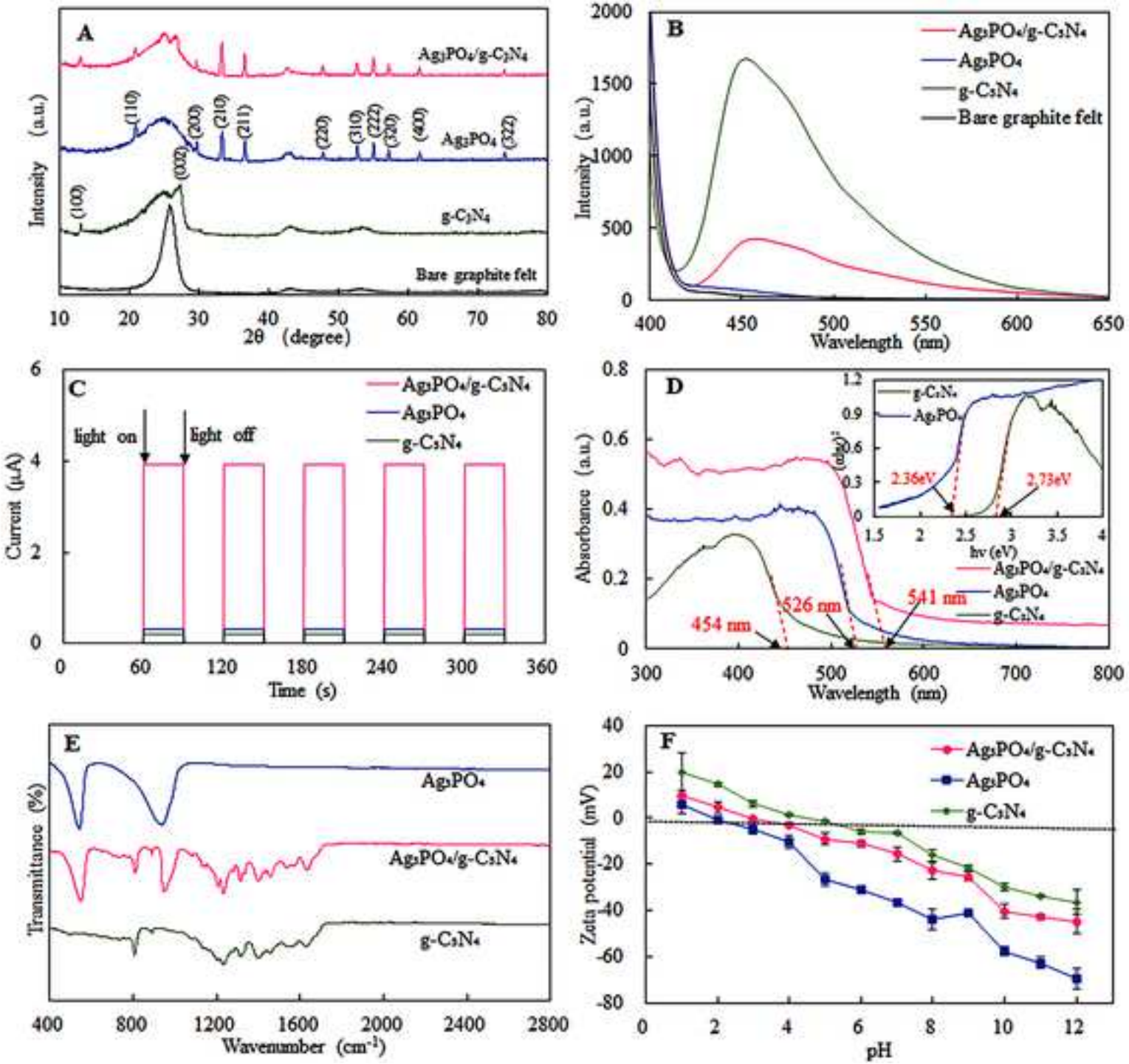

Figure 2

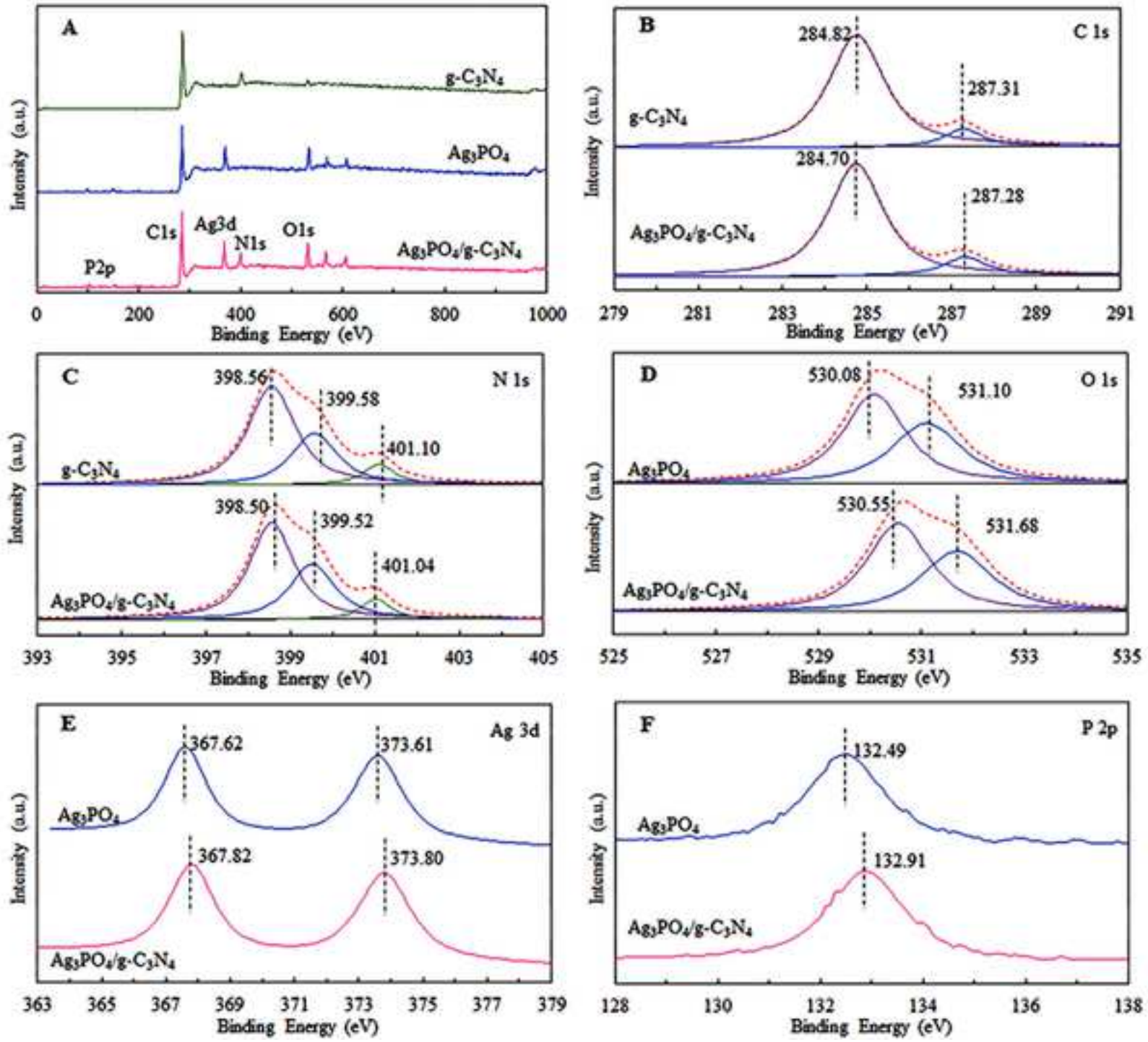

Figure 3

Click here to access/download;Figure;Fig. 3.tif

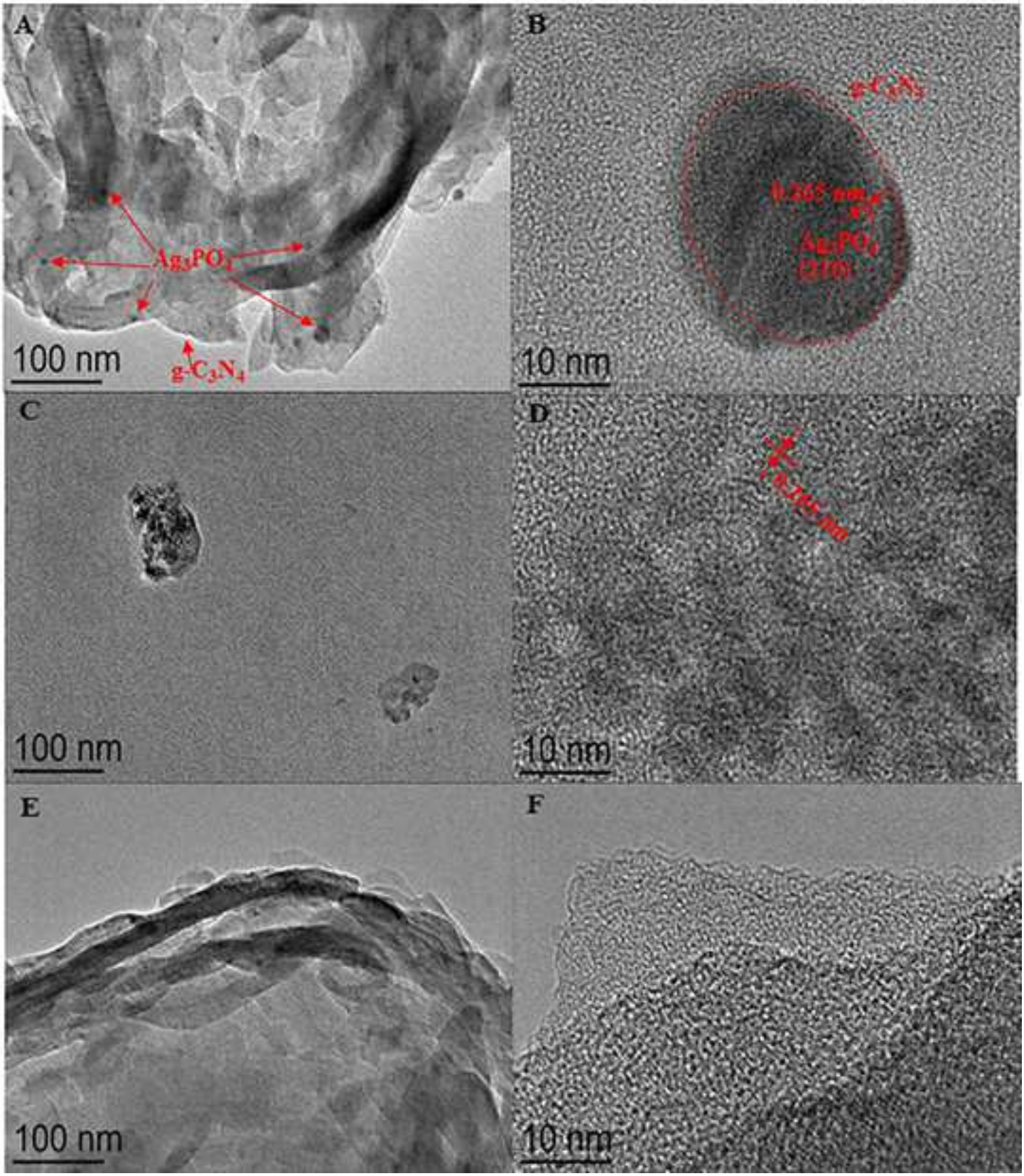

Figure 4

Click here to access/download;Figure;Fig. 4.tif

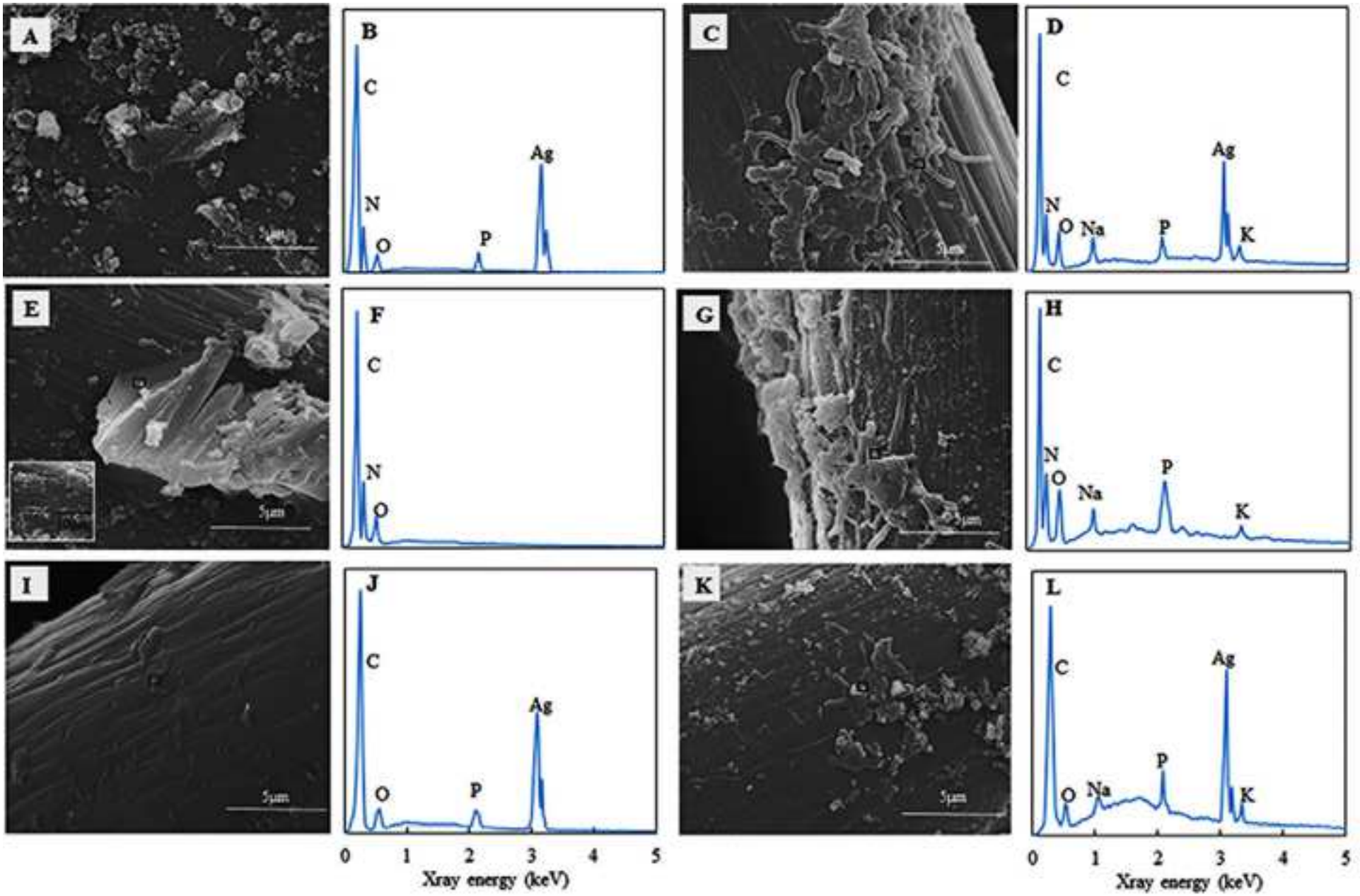

Figure 5

Click here to access/download;Figure;Fig. 5.tif

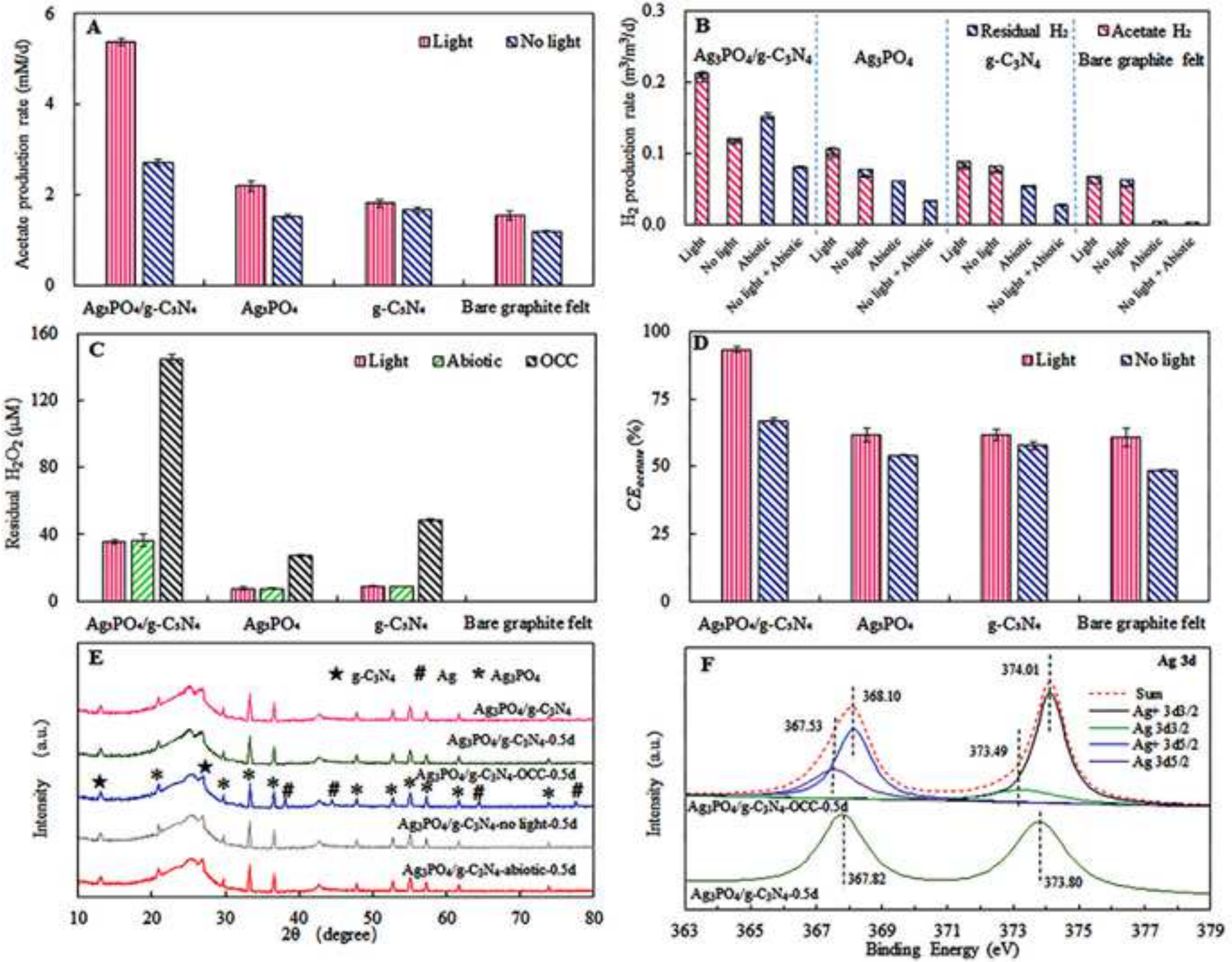

Figure 6

Click here to access/download;Figure;Fig. 6.tif

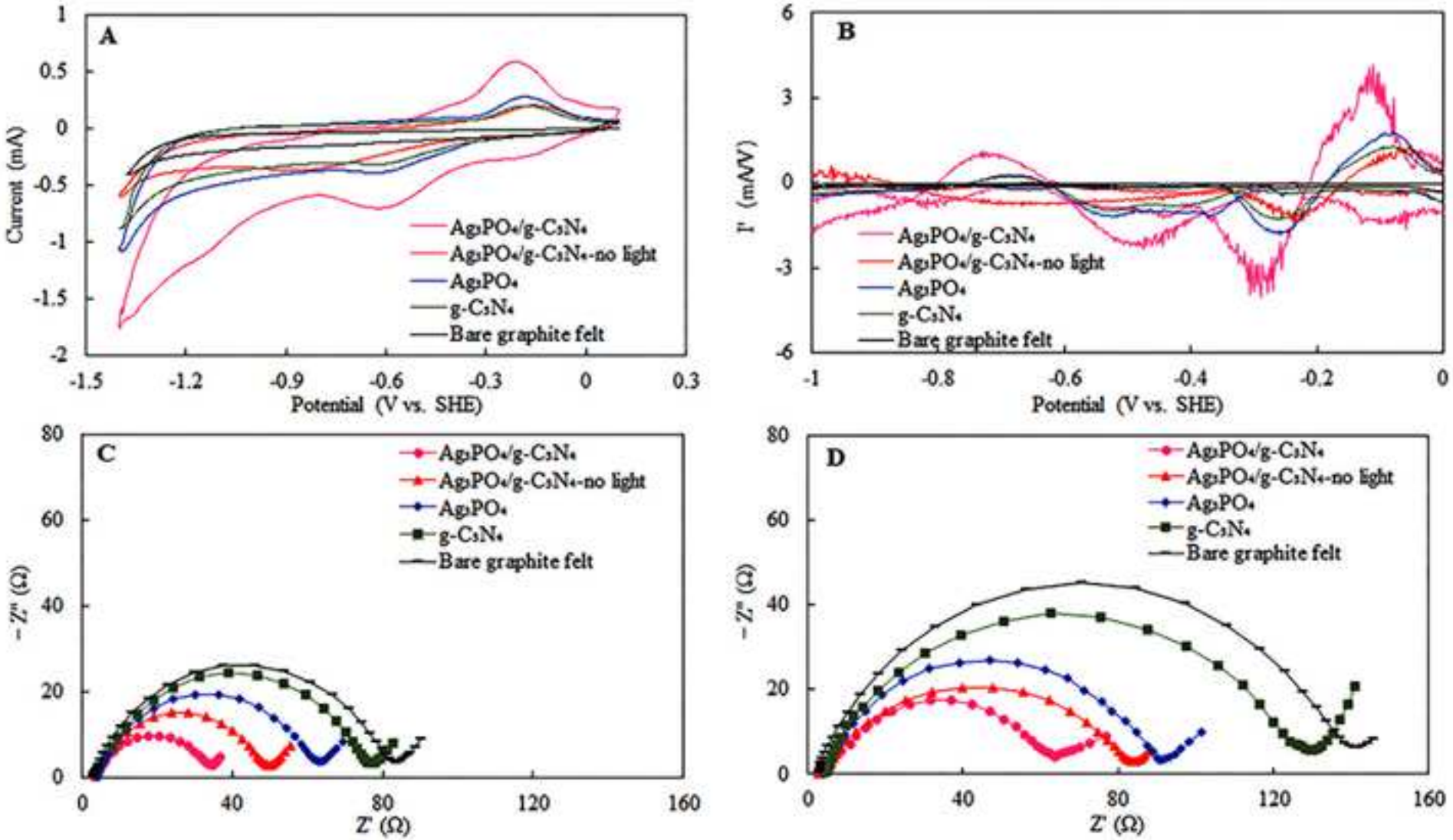

Figure 7

Click here to access/download;Figure;Fig. 7.tif

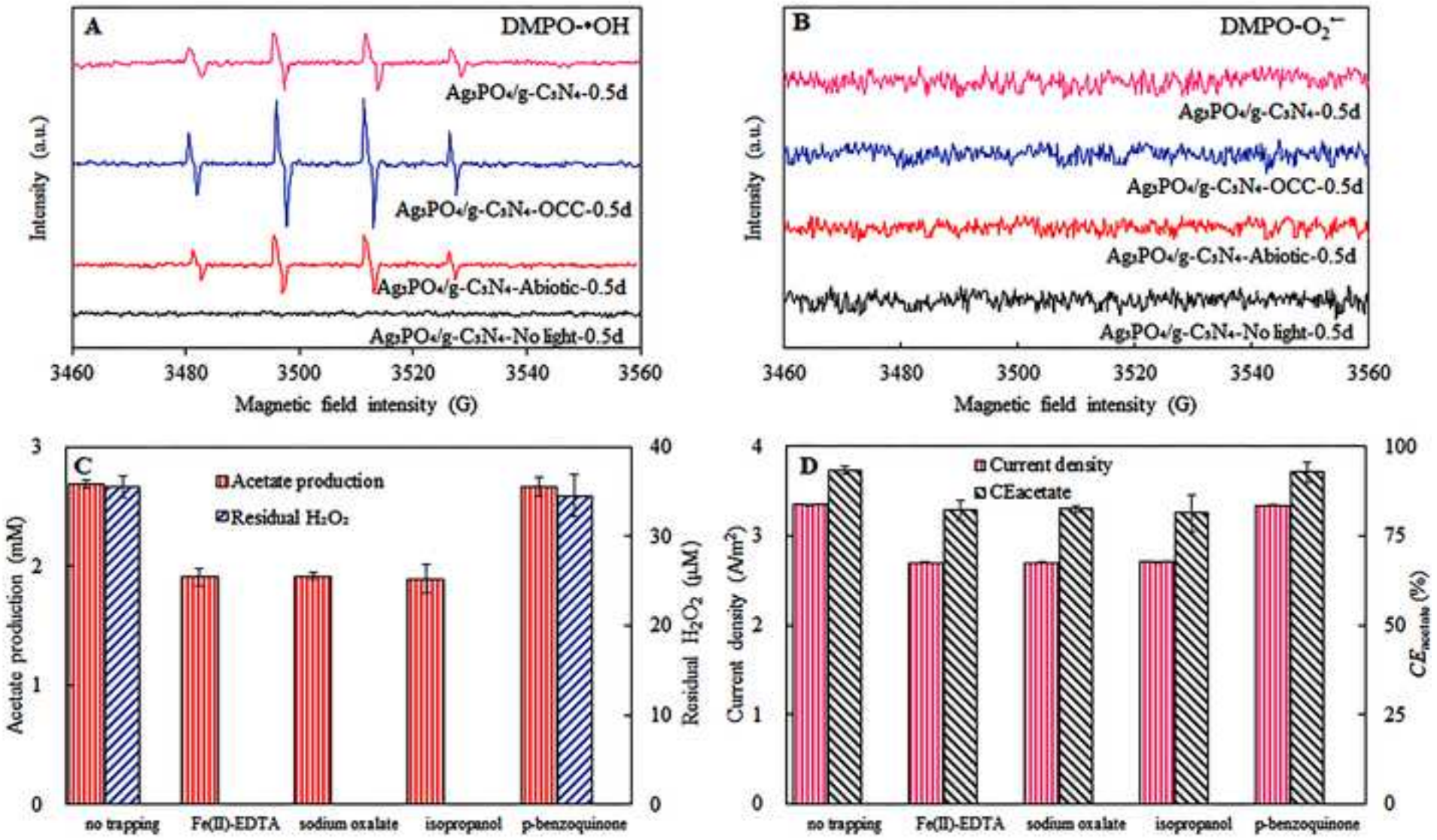

Figure 8

Click here to access/download;Figure;Fig. 8.tif

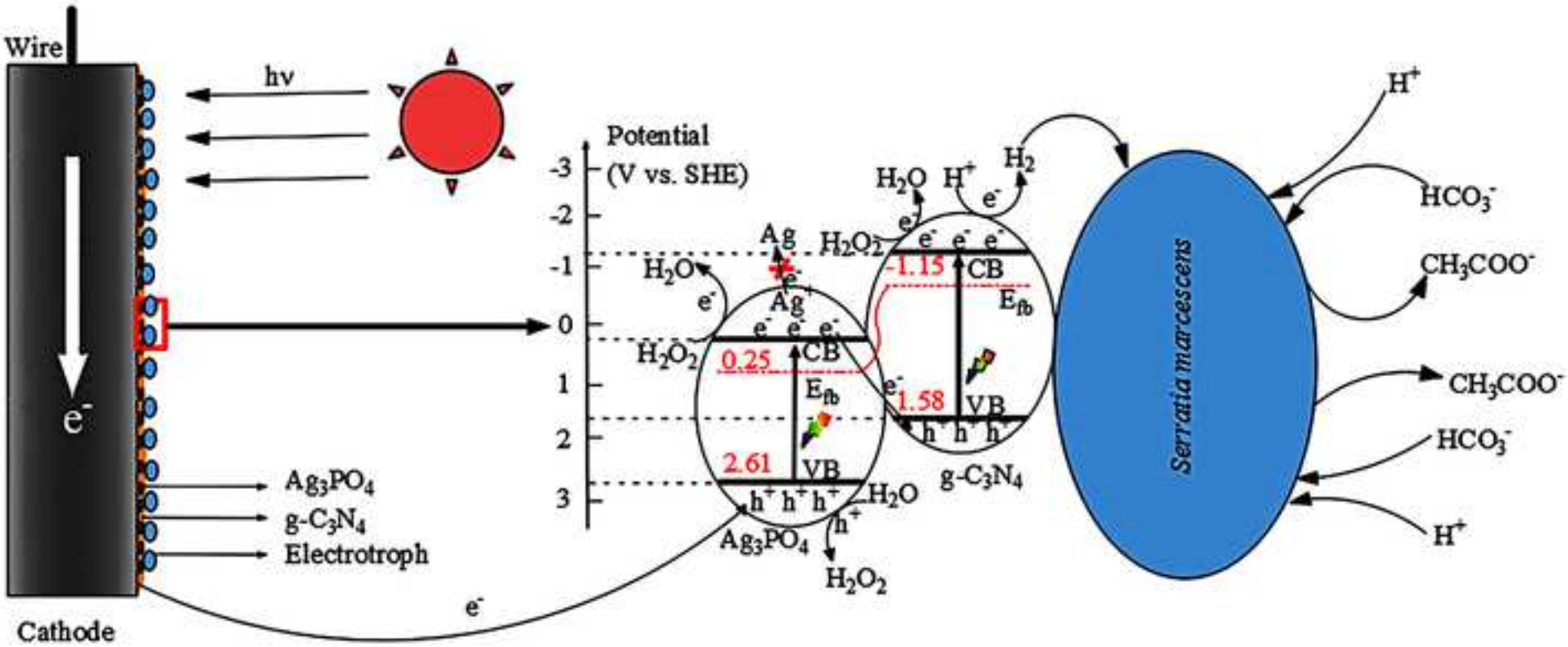

Figure 9

Click here to access/download;Figure;Fig. 9.tif

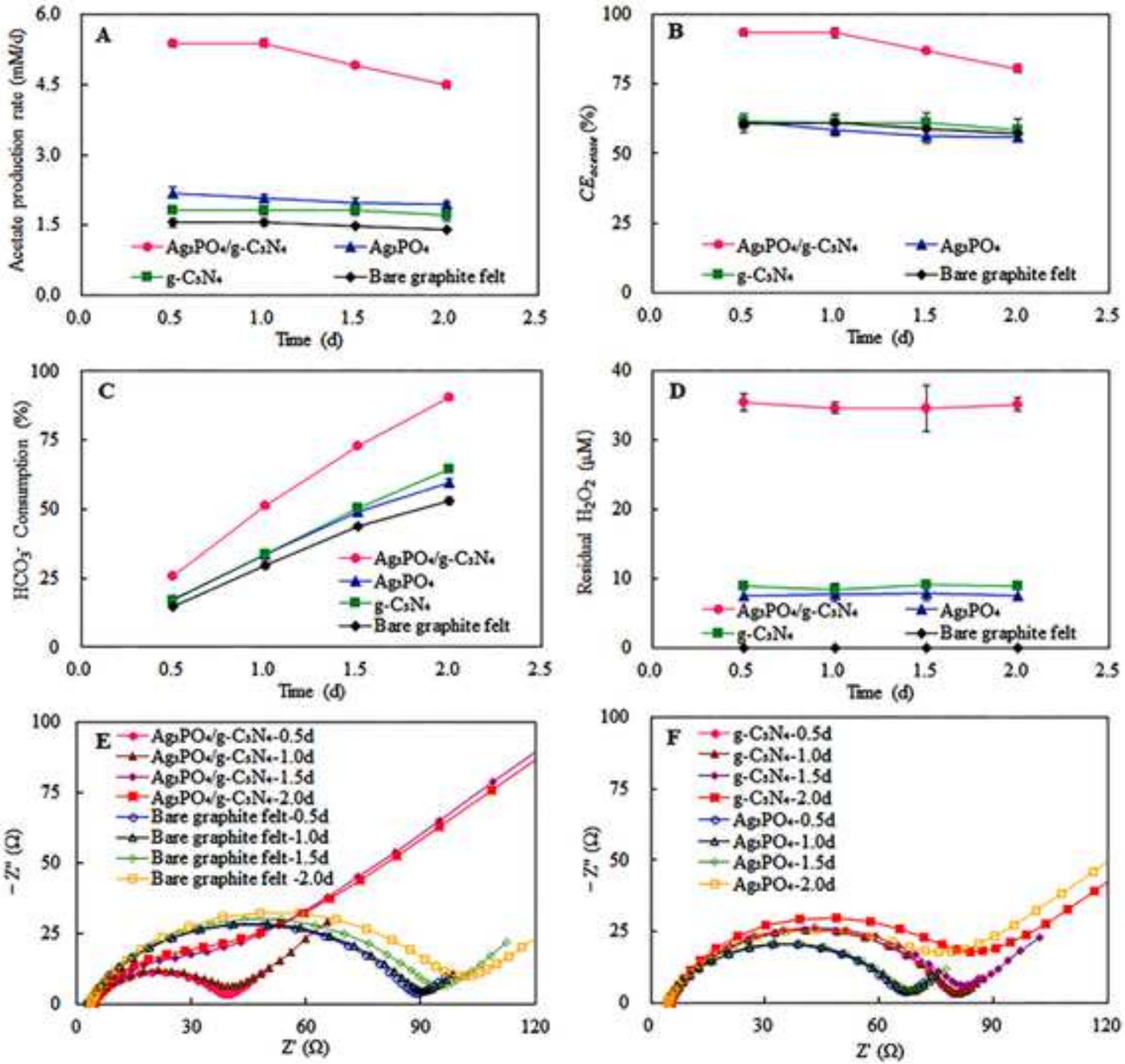

Figure 10

Click here to access/download;Figure;Fig. 10.tif

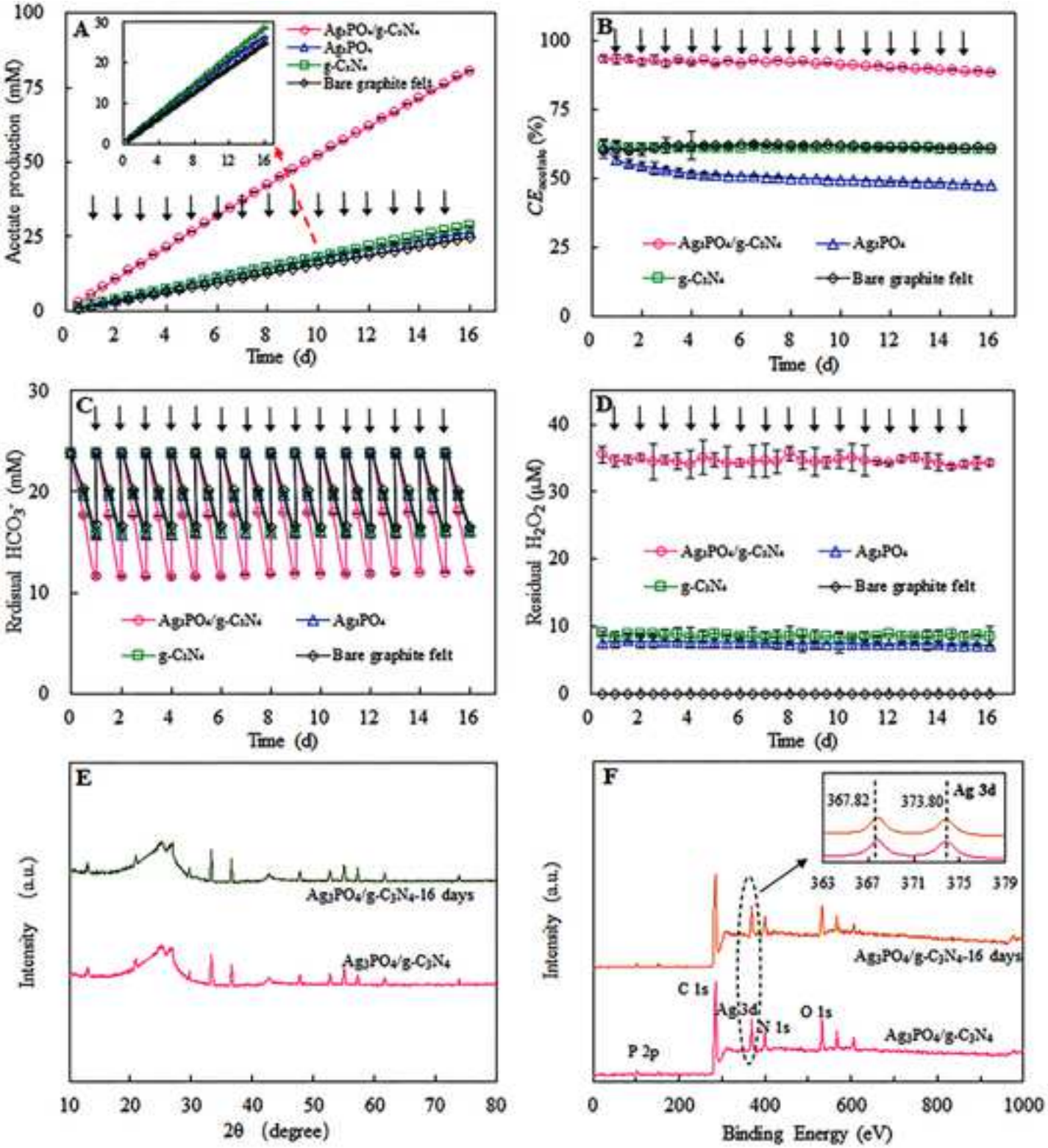

*Graphical Abstract

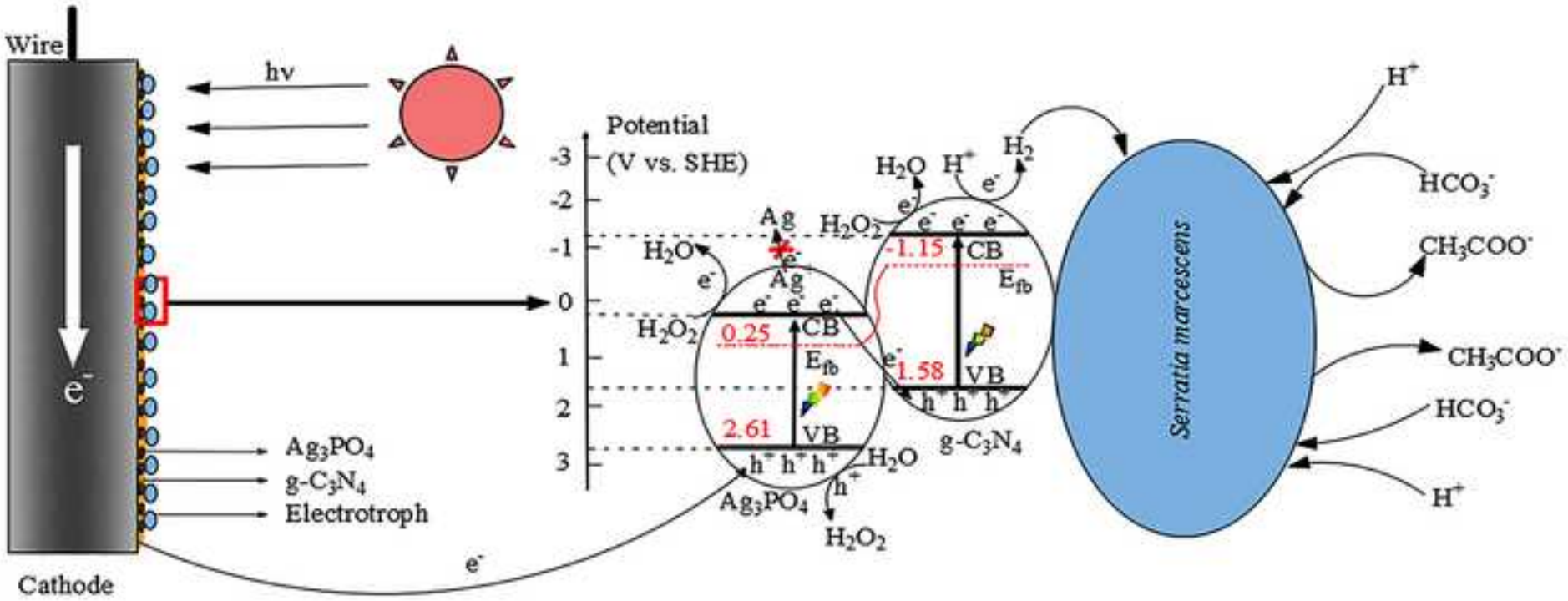

Highlights

- Ag_3PO_4/g-C_3N_4 and *S. marcescens* catalyze acetate production in photo-assisted MES;
- H_2O_2 produced in-situ under anaerobic conditions prevents photoetching of Ag_3PO_4;
- Ag_3PO_4/g-C_3N_4 Z-scheme heterojunction enhances electron-holes separation;
- Photo-induced electrons on conduction band of semiconductor enhances H_2 production;
- Photo-generated holes favors higher current and higher rates of acetate production.